THE MODELING AND SIMULATION OF HIGH-SPEED CONTINUOUS AND DISCONTINUOUS CHIP FORMATION IN THE MACHINING OF AISI 4340 STEEL

THE MODELING AND SIMULATION OF HIGH-SPEED CONTINUOUS AND DISCONTINUOUS CHIP FORMATION IN THE MACHINING OF AISI 4340 STEEL

BY

ERIC ARAUJO, B. ENG.

SEPTEMBER 2000

A THESIS

SUBMITTED TO THE SCHOOL OF GRADUATE STUDIES

IN PARTIAL FULFILLMENT OF THE REQUIRMENTS

FOR THE DEGREE

MASTERS OF ENGINEERING

MCMASTER UNIVERSITY

Masters of Engineering (2000) McMaster University

(Mechanical Engineering Department) Hamilton, Ontario

TITLE: THE MODELING AND SIMULATION OF HIGH-SPEED CONTINUOUS AND DISCONTINUOUS CHIP FORMATION IN THE MACHINING OF AISI 4340 STEEL

AUTHOR: Eric Araujo, B.Eng. (Department of Civil Engineering)
(McMaster University, Hamilton, Ontario)

SUPERVISOR: Dr. M. A. Elbestawi, Professor, Mechanical Engineering Department
Dr. D. R. Metzger, Professor, Mechanical Engineering Department

NUMBER OF PAGES: ii, 110

ABSTRACT

Throughout engineering history, metal cutting technology has been pushed to keep pace with the development of stronger and more difficult to cut materials. With the advent of robust machining technology, the finish cutting of hardened materials at high speeds and extreme conditions has become possible. As we push the thresholds of our technology, the need for a deep understanding of the processes at work in metal cutting in order to predict limit states has become clear.

The prediction of machining processes began with models that described the problem qualitatively. The principals and assumptions used within these laid the foundations for further theoretically based empirical models. With the advent of computationally based numerical modeling, predictive modeling of metal cutting processes using elasto-plastic based simulation has brought a new perspective to the field. The development of finite element modeling techniques capable of modeling both continuous and discontinuous chip formation has become a subject of considerable research effort.

The present work focuses on the study and development of explicit transient finite element techniques used to simulate the orthogonal machining of hardened steel under various cutting conditions producing both continuous and discontinuous chips. Metal cutting involves a diversity of complex physical phenomenon such as large strain and strain rate plasticity, high temperature contact and friction conditions, material failure, adiabatic shear localization, and thermo-mechanically based deformation. The numerical

modeling of these processes in orthogonal machining operations is the primary focus of this work. The effects of cutting conditions on chip morphology and the finished workpiece are investigated and resulting phenomenon are explained in terms of numerically based stress analysis. Benchmarking comparisons with literature and commercial modeling software simulations are made and quantified in terms of strains, temperatures, residual stresses, and the various components of stress. Future directions and issues are outlined and recommendations are made.

Solution stability of the finite element solver applied to machining was quite low due to the lack of an adaptive remeshing scheme and deficiencies in the contact algorithm. Thermal mechanical coupling and remeshing are currently being implemented. Future avenues include methods of surface generation without volumetric losses, the application of friction based on wear data, and the application of machining simulations to oblique three-dimensional cutting operations.

ACKNOWLEDGMENTS

The author wishes to express his sincere gratitude to his research supervisors, Dr. M. A. Elbestawi and Dr. D. R. Metzger for their continual support and guidance throughout this research. I want to thank them both on a personal level for the opportunity and future they helped create for me by supporting my studies, and for the confidence and outlook they taught me that can only be inspired by mentors. I would like to thank all my family, my father, my brother, and my mother, for all the support they gave without a moments thought throughout my life. Without them I would be lost without purpose, as they always believed in me without question or doubt. I would like to thank Farid Abrari and Greg Jacklin for the untiring support and guidance they offered as both friends and teachers. They helped inspire laughter and drive when all hope seemed lost, and reality and composure when optimism prevailed. I would like to thank Rich for our musical escapes from engineering, Ed for his conversations over a cup O' joe, and Dwayne for listening to the weekly FEA blues hour. I would like to thank Don for the seemingly hundreds of hours I spent in his office, as he always took the time and interest to converse as a friend and explain as a teacher. I want to thank both Shelley and Greg for being both family and friend, as they always managed to inspire and support without question or expectation. I would like to thank all the friends I made both outside and inside the research lab during my studies at McMaster, and to all my friends in the D.U.I. back home, I send my thanks for your support and guidance throughout the years.

For My Mother

TABLE OF CONTENTS

LIST OF FIGURES

LIST OF TABLES

CHAPTER 1

INTRODUCTION

The machining of metal is a process that involves irreversible material removal from a workpiece. Elevated temperatures, high strain rates, complex fracture mechanics, and large deformations in the plastic and elastic range make metal cutting a highly non-linear process. This extreme non-linearity causes heightened solution sensitivity to initial conditions and assumptions. This inherent instability results in a low predictive horizon for metal machining modeling. Early attempts were made to model this complex problem through the use of experimental data, but the lack of material properties at high temperatures and strain rates have proved to be a difficult barrier. Temperature and strain rate are highly non-linear and time dependant in shear localized regions, and hence traditional empirical and theoretical solutions can only be very specific to cutting conditions and materials. This limitation causes reduced or non-applicable versatility and accuracy when applied to problems with different initial conditions.

The introduction of the finite element method in the 1950's made it possible to solve approximately non-linear differential equations by discretizing with finite freedoms or boundary conditions (Shirakashi and Maekawa, 1996). Finite element models began with 2-D solutions to continuous chip formation, moving slowly to continuous chip formation in three dimensions and discontinuous chip formation in two dimensions as computer power has increased. It is now possible to begin to model metal machining, but the accuracy of solutions is still highly dependent on assumptions used to simulate the mechanics of the process. The formation of discontinuous chips in an elasto-plastic manner is of particular interest due to its applicability to high speed machining.

Partial/gross fracture in a brittle/ductile manner or shear localization take place in the chip formation of materials having poor ductility and or thermal sensitivity such as beta brass, titanium, and nickel based super alloys (Obikawa and Sasahara, 1997). The discontinuous chips produced by these materials in high speed machining exhibit cracks and evidence of shear localization. These cracks and zones of high residual stress will also appear on the finished surface, hence degrading the quality and material properties of the finished workpiece surface and subsurface.

Finite element models must use an accurate interpretation of the mechanics of the metal cutting process to be viable and versatile in practical application. In a finite element model, material properties can be handled as functions of strain, strain rate, and temperature. The interaction between the chip and the tool can be modeled in both sliding and sticking behaviour. Cutting force, feed force, chip geometry, local stress, and temperature distributions can also be obtained from this type of analysis, making it an ideal tool for machining process optimisation (Zhang and Bagchi, 1994). Material behaviour has been modeled as rigid-plastic, elasto-plastic, visco-plastic, and elastic-visco-plastic. Assuming a plane-strain condition, an orthogonal cut neglects the dynamic plastic flow involved in an oblique three-dimensional metal cutting operation. The three dimensional influence of the tool on the workpiece also has an important effect on the cutting process and residual forces, particularly at higher cutting speeds and aggressive feeds.

Strain rate and temperature are often neglected in finite element models, and this causes severe limitations in the applicability to machining at higher speeds. The lack of material properties at high strain rates and temperatures and the difficulty of numerical implementation is often the justification behind these simplifications in the modeling of discontinuous chip formation. Difficulties also arise due to the lack of reliable criterion for ductile fracture in large plastic deformation problems involving high normal and hydrostatic forces. The importance of node separation criterion, fracture initiation, and crack propagation in models are paramount in defining the shape of the formed chip, cutting forces, as well as the residual properties of the chip and workpiece. In essence, the lack of material data, the difficulty of numerical implementation, and computational power currently limit the application of traditional finite element models in the everyday analysis of metal machining processes.

The development of a machining process involves a considerable amount of capital investment and time. Cutting conditions like tool geometry and cutting speed directly influence the formation of chips, cutting forces, tool life, and finished workpiece quality. The definition of optimal ranges of process parameters is critical in the effective implementation of a machining process to production. Computational modeling of machining processes offers a considerable reduction in the number of iterations involved in the design of a production floor cutting process. Finished workpiece properties such as finish and residual stress are also predicted, offering feedback for the design engineer on the effects of the manufacturing process on a component being designed. Hence, considerable savings in the optimisation of both the design and manufacturing stages of a component are offered through the development of this work.

CHAPTER 2

MACHINING AND MECHANISMS OF CHIP FORMATION

Traditional metal cutting processes involve the removal of unwanted material through the use of single or multiple cutting edges. This process is used to produce a desired profile from a bulk section of workpiece material. Different metal cutting operations include turning, milling, drilling, broaching, and grinding. The chips produced by metal cutting operations can be generally categorized as continuous, discontinuous, or continuous with a built up edge (BUE) (Ernst, 1938), where current works suggest more comprehensive classifications within each of these groupings. Despite complex cutting tool geometries and cutting conditions, most cutting operations can be described and simplified as either oblique or orthogonal cutting operations. Oblique cutting operations are more representative of most industrial applications wherein the cutting edge of the tool is inclined with respect to the axis perpendicular to cutting direction velocity. Due to the complexity of three-dimensional geometries and mechanistic processes, this type of operation is difficult to fully quantify and represent using current analytical and numerical modeling techniques.

Orthogonal cutting operations have no cutting edge inclination with respect to the z-axis perpendicular to the cutting velocity. This type of operation can be idealized as a predominately plane strain type of deformation, and henceforth can be modeled as a two-dimensional deformation process where strain has no variation in the neglected Zdimension. This type of idealization can then be used to model more complex processes by representing the problem as discretized orthogonal sections across a three-dimensional oblique cutting edge. It follows that all current acknowledged analytical chip formation models use this generalized plane strain assumption. Orthogonal cutting conditions also tend to produce experimental results that are easier to compare with predictive models.

2.1 Continuous Chip Analytical Models

Continuous chips are more commonly produced when machining more ductile metals such as aluminum, mild steels, copper, and wrought iron. Less ductile materials can also produce continuous chips but often only do under a range of specific cutting conditions. This type of chip formation involves deformation that is predominately a shearing mechanism without any macroscopic fracture. Because of this continuous chip formation is often regarded and modeled as a steady state process. There are two major types of model that are used to describe the continuous orthogonal cutting process being the slip-line model (Lee and Shaffer, 1951) and the shear plane model (Merchant, 1945).

2.1.1 Slip Line Model

The slip line model as outlined by Lee and Shaffer in 1951 uses a slip line field technique to solve the system in terms of a plasticity problem. This requires the assembly of a slip-line field. This usually consists of two mutually orthogonal families of lines in the directions of the maximum shear stresses as shown in figure 2.1(a). This model assumes a rigid-plastic material that is independent of temperature and strain rate where shear is the governing deformation mechanism. This model also assumes constant plastic deformation within the region A-B-C and a maximum shear along the line A-B that inherently implies full contact between the chip and the tool. Based on these assumptions, a subdivision such as element 1 is stress free on its surface *b* on A-B and areas *a* and *c*. Figure 2.1(b) shows a Mohr's circle diagram of element 1 in which the zero stresses of face *b* and the maximum stresses of *a* and *b* are plotted. Element 2 is located on the chip/tool interface and its faces *d* and *f* are on the slip-lines I and II respectively. The face *e* experiences tensile stresses due to friction and is inclined from the slip-line I at an angle *P*. The analysis of the friction and normal forces and the shear and normal stresses shows

$$\mu = \frac{F}{N} = \frac{\tau}{\sigma} = \tan(\beta) \qquad (2.1)$$

where μ is the friction coefficient. From the Mohr's circle, the relation between the angles of the slip-lines I and the friction angle can be expressed as

$$\eta = 45 - \beta \qquad (2.2)$$

The friction angle can be expressed in terms of the shear and rake angles as

$$\eta = \phi - \alpha \qquad (2.3)$$

and it follows that the solution for the shear plane angle can be found as

$$\phi = 45 - \beta + \alpha \qquad (2.4)$$

This model is useful but is limited by the fact that it uses a free chip hypothesis that neglects the effects of elastic forces in the chip and workpiece on the plastic deformation field. This model also assumes an *a priori* relationship between the maximum shear stress and the hydrostatic stress.

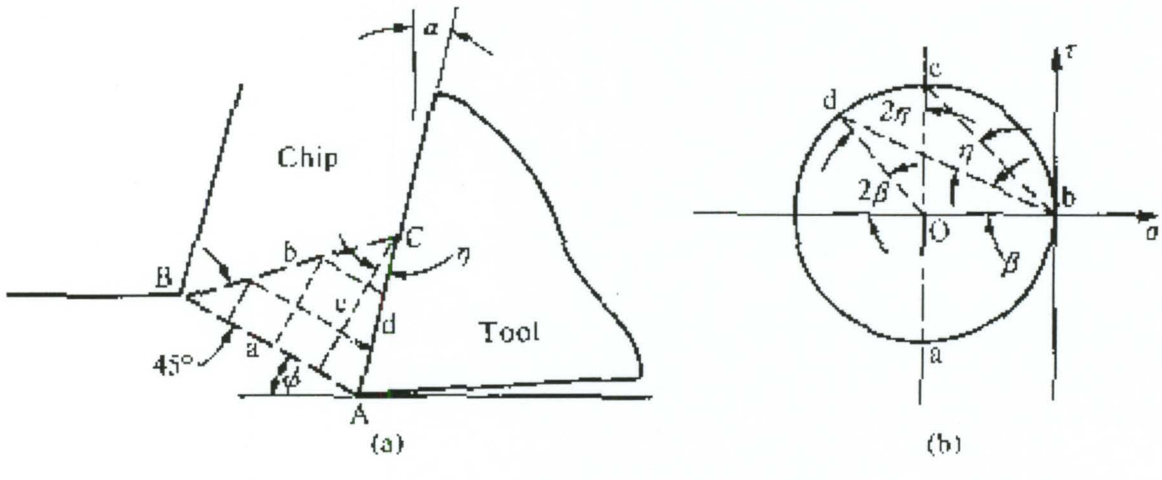

Figure 2.1 Ideal plastic solution for stress field at tool point. (a) Slip line field. (b) Mohr's circle diagram for field ACB (Lee and Shaffer 1951).

2.1.2 Shear Plane Model

The shear plane model is one that infers that there is absolutely no inhomogeneous strain by assuming that the material behaves in a homogeneous fashion. This is the first of many assumptions that this model uses which are listed as follows (Shaw, 1984):

1. The tool is perfectly sharp and there is no contact along the clearance edge.
2. The shear surface is a plane extending upward from the cutting edge.
3. The cutting edge is a straight line extending perpendicular to the direction of motion and generates a plane surface as the work moves past it.

4. The chip does not flow to either side (plane strain).
5. The depth of cut is constant.
6. The width of the tool is greater than that of the workpiece.
7. The workpiece moves relative to the tool with a uniform velocity.
8. A continuous chip is produced with no built-up edge.
9. The shear and nominal stresses along shear plane and tool are uniform.
10. The flow has a rigid-perfectly-plastic constitutive material model

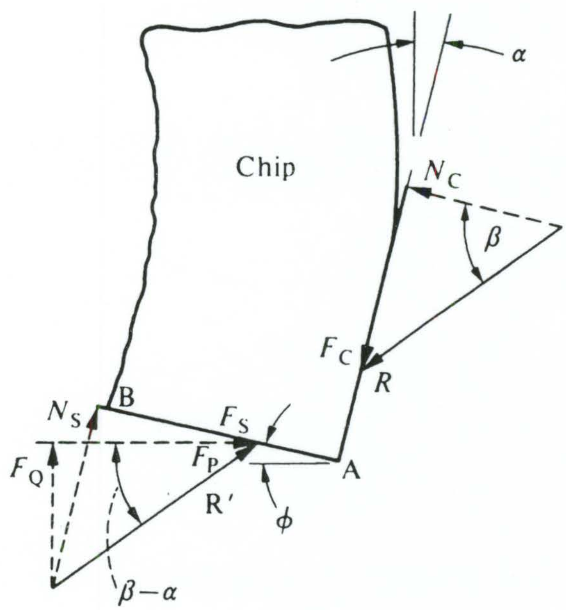

Figure 2.2 Free body diagram of a chip (Shaw, 1984).

Merchant's shear plane model of orthogonal cutting published in 1945 was the first to begin to accurately describe this cutting process. As shown in figure 2.2, equilibrium is assumed between the force between the tool face and the chip R and the force between the workpiece and the chip on the shear plane R'. R' is then resolved into

F_P and F_Q which corresponds to the forces obtained while using a force dynamometer. These forces are then projected onto the shear plane and resolved into

$$F_S = F_P \cos\phi - F_Q \sin\phi \qquad (2.5)$$

$$N_S = F_Q \cos\phi + F_P \sin\phi = F_S \tan(\phi + \beta + \alpha) \qquad (2.6)$$

where F_S is a shearing force and N_S is a force normal to the shear plane. These are then projected onto the rake face and resolved into

$$F_C = F_P \sin\alpha + F_Q \cos\alpha \qquad (2.7)$$

$$N_C = F_P \cos\alpha - F_Q \sin\alpha \qquad (2.8)$$

Where F_C is tangential and N_C is normal to the rake face. The mean tool face coefficient of friction can then be solved as

$$\mu = \frac{F_C}{N_C} \qquad (2.9)$$

Stresses can be determined as

$$\tau = \frac{(F_P \cos\phi - F_Q \sin\phi)\sin\phi}{bt} \qquad (2.10)$$

$$\sigma = \frac{N_S}{A_S} = \frac{(F_P \cos\phi + F_Q \cos\phi)\sin\phi}{bt} \qquad (2.11)$$

where τ and σ are the mean shear stress and the mean normal stress on the shear plane respectively. By differentiating equation 2.11 with respect to ϕ and equating to zero,

$$\phi = 45 - \frac{\beta}{2} + \frac{\alpha}{2} \qquad (2.12)$$

where it is assumed that both R' and β are independent of ϕ. The cutting ratio is defined as

$$r = \frac{t}{t_C} = \frac{l_C}{l} \tag{2.13}$$

where t and t_C represent the chip thickness measured experimentally before and after the cut. The shear plane angle ϕ can then be solved as

$$\tan\phi = \frac{r\cos\alpha}{1 - r\sin\alpha} \tag{2.14}$$

where α is the rake angle of the tool. The shear angle can also be derived as

$$\phi = \frac{\cot^{-1}(K)}{2} - \frac{\beta}{2} + \frac{\alpha}{2} \tag{2.15}$$

where $\cot^{-1} K$ is the machining constant C introduced by Merchant.

The mean shear strain γ in cutting can be calculated as

$$\gamma = \frac{\cos\alpha}{\sin\phi\cos(\phi - \alpha)} \tag{2.16}$$

The mean shear velocity V_S on the shear plane can be calculated as

$$V_S = \frac{\cos\alpha}{\cos(\phi - \alpha)} V \tag{2.17}$$

where V is the cutting speed. The strain rate $\dot{\varepsilon}$ can be calculated as

$$\dot{\varepsilon} = \frac{\Delta S}{\Delta y \Delta t} = \frac{V_S}{\Delta y} \tag{2.18}$$

where Δy is the thickness of the primary shear zone.

When metal is cut orthogonally, the total energy consumed per unit time U is

$$U = F_p V \tag{2.19}$$

The total energy per unit volume of metal removed u is

$$u = \frac{U}{Vbt} = \frac{F_P}{bt} \tag{2.20}$$

where b is the width of the cut.

The amount of friction energy generated per unit volume u_S can be calculated as

$$u_F = \frac{F_C V_C}{Vbt} = \frac{F_C r}{bt} \tag{2.21}$$

When two new surfaces are created, there is a small amount of energy used. This surface energy per unit volume u_A generated can be calculated as

$$u_A = \frac{(T)(2Vb)}{Vbt} = \frac{2T}{t} \tag{2.22}$$

The momentum energy per unit volume u_M can be calculated as

$$u_M = \left(\gamma'/_g\right) V^2 \gamma^2 \sin^2 \phi \tag{2.23}$$

where

$$\gamma'/_g \tag{2.24}$$

is the mass density of the material. It is found in practice that the surface and momentum energies are negligible in comparison with the shear and friction generated in orthogonal cutting tests. It is also found that the friction energy produced in steady state turning operation is approximately one third of the shearing friction energy (Shaw, 1984). Continuous chip models provide a very poor approximation for cutting with discontinuous chips. Hence, considerable work has been done in the attempt to model discontinuous chip formation.

2.2 Discontinuous Chip Analytical Models

Discontinuous chips are produced when machining materials with poor ductility and or thermal sensitivity such as beta brass, titanium, hardened steels, and nickel based super alloys (Obikawa and Sasahara, 1997). This chip formation process involves partial/gross macroscopic fracture in a brittle/ductile manner as well as pronounced shear localization. High-speed machining operations also tend to produce segmented chips in many materials when preformed using more aggressive feeds and speeds. There are currently two distinct schools of thought in the analytical description of the discontinuous chip formation process. The first adopts the view that the root cause of saw-tooth chip formation is cyclic crack formation. This type of model is thoroughly described in different forms by both Shaw (1998) and Elbestawi (1996). The second type of model adopts the view that adiabatic shear localization is the root cause of discontinuous chip formation. This type of model was first introduced by Recht (1964) and has been further developed in detail by Komanduri (1997).

2.2.1 Cyclic Crack Model

The periodic crack model assumes that the crack initiates at the workpiece surface and propagates down along the shear plane towards the tool tip. Once this crack has been formed, sites of shear localization may or may not then develop. Shaw defines the four types of cyclic chips as discontinuous, wavy, those produced with a BUE, and saw-tooth (Shaw, 1998). Figure 2.3 illustrates these four different types of chips.

Elbestawi (1996) outlines a cyclic chip model in which chip formation starts with the initiation of Mode I brittle fracture at the free surface based on an experimentally determined surface layer strain energy failure criterion. This crack then propagates towards the tip of the tool. The direction of crack propagation is determined using a strain energy density criterion such that the surface layer energy reaches a maximum at the minimum applied pressure. The crack then ceases to propagate as it reaches the region of high plastic deformation and compressive pressure near the tool tip. The chip region is then caught between the tool rake face and the crack. It is then extruded up the rake face with the highly plastically deformed material below it, and a cyclic chip is formed.

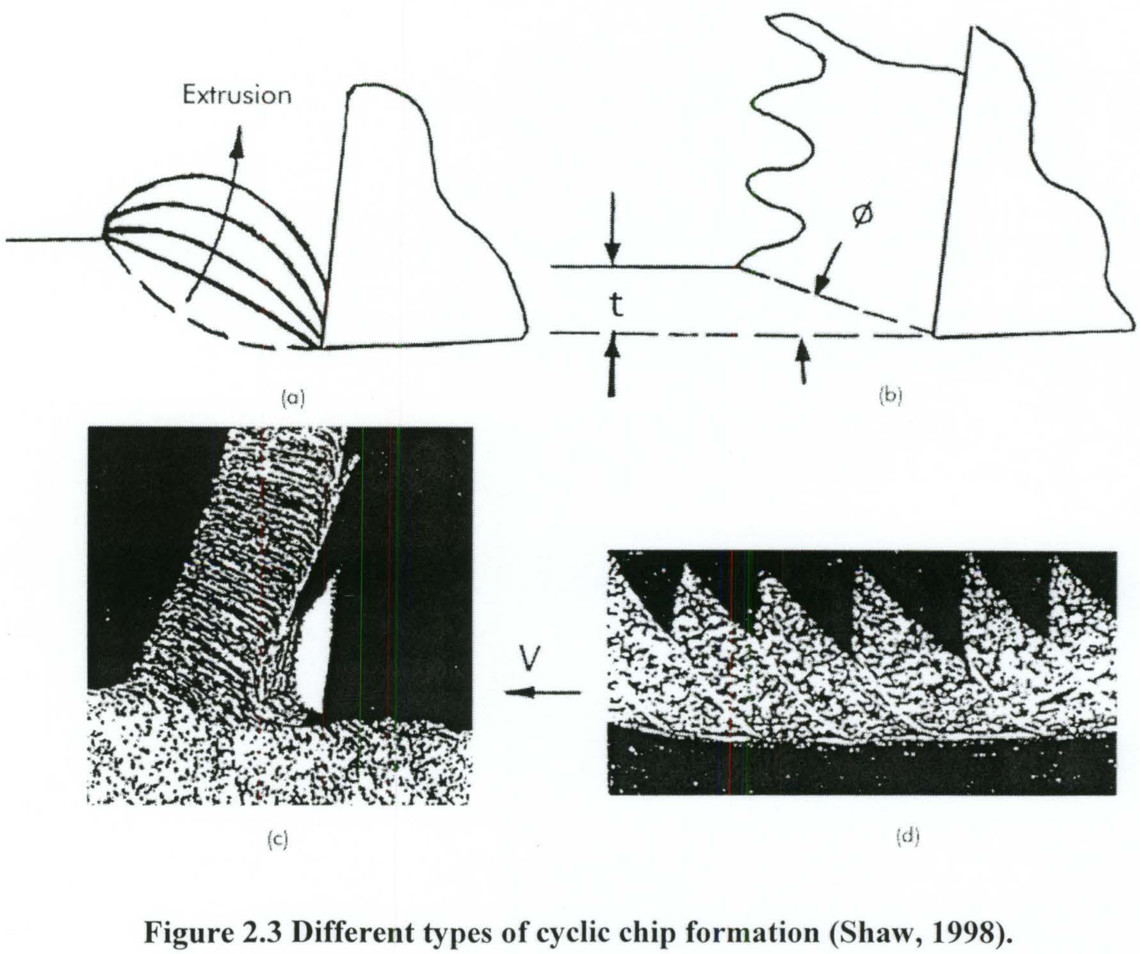

Figure 2.3 Different types of cyclic chip formation (Shaw, 1998).

Discontinuous chips as outlined by Shaw (1998) (figure 2.3(a)) are characterized by the formation of a tensile crack initiating from the tool tip and propagating into a shear crack that intersects the workpiece surface at approximately 45°. The chip is then extruded up along the rake face and a new cyclic crack is formed when the cutting force reaches a critical value. Each of these segments is then completely ejected from the cutting process by the elastic release of energy due to cracking. Figure 2.3(b) illustrates the morphology of a wavy chip. Some type of cyclic phenomenon, such as regenerative chatter or a BUE causes this type of chip formation. In a case where a BUE is present, as shown in figure 2.3(c), the BUE is actually doing the cutting instead of the real tool profile. This cyclic formation and the size of a BUE under specific cutting conditions leads to a large increase in the surface roughness of the machined surface. Finally, figure 2.3(d) shows the saw-tooth chip morphology that current discontinuous models are focused upon. This type of chip exhibits highly localized cracking and deformation in bands and very little evidence of plastic strain in the bulk of the chip segment.

The majority of experimental research has concentrated on materials such as titaniums (e.g. Ti-6Al-4V), high strength steels (e.g. AISI 4340), and nickel based super alloys (e.g. Inconel 718). Figure 2.4 and figure 2.5 both show a saw-tooth chip just after crack formation with the current segment extruded a small distance DC_1. The gross cracked (*GC*) region of the chip extends from C_2 to D_2 and the micro cracked (*MC*) region runs from D_2 to T as shown in figure 2.5.

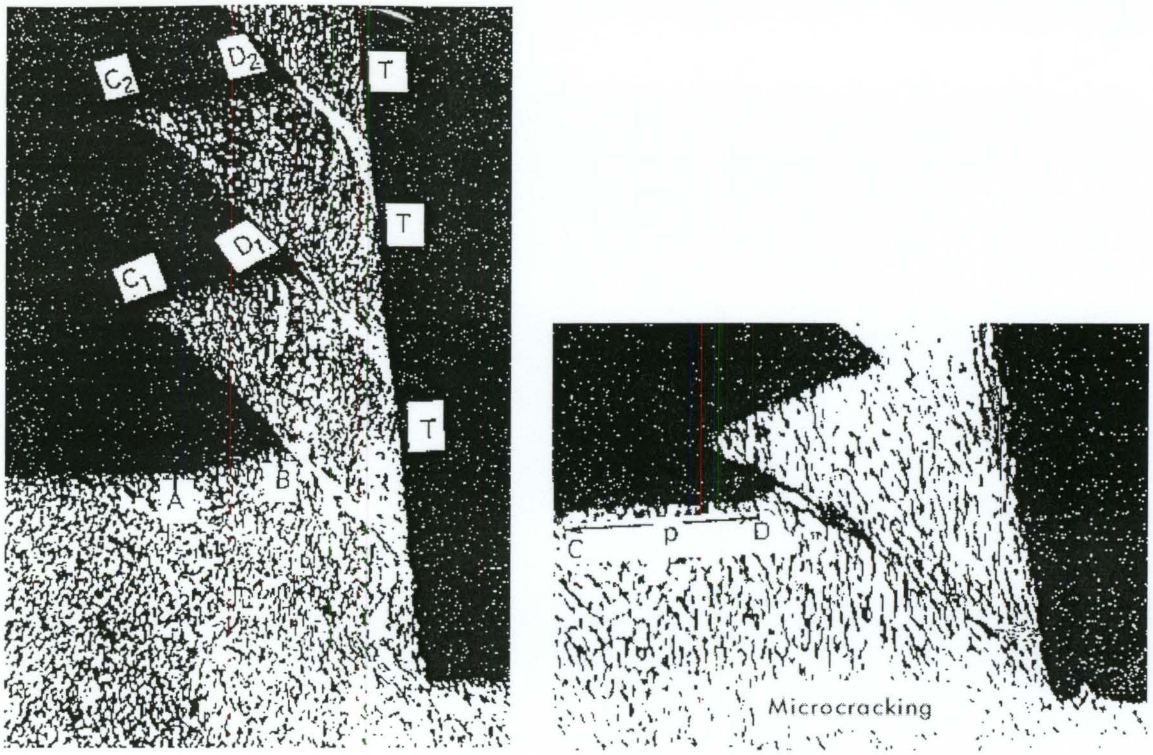

Figure 2.4 Quick stop photomicrographs of 6Al-4V titanium alloy. (a) Halfway between cyclic cracks. (b) Shortly after formation of a crack showing the extent of the *OG* and *MC* regions (Shaw, 1998).

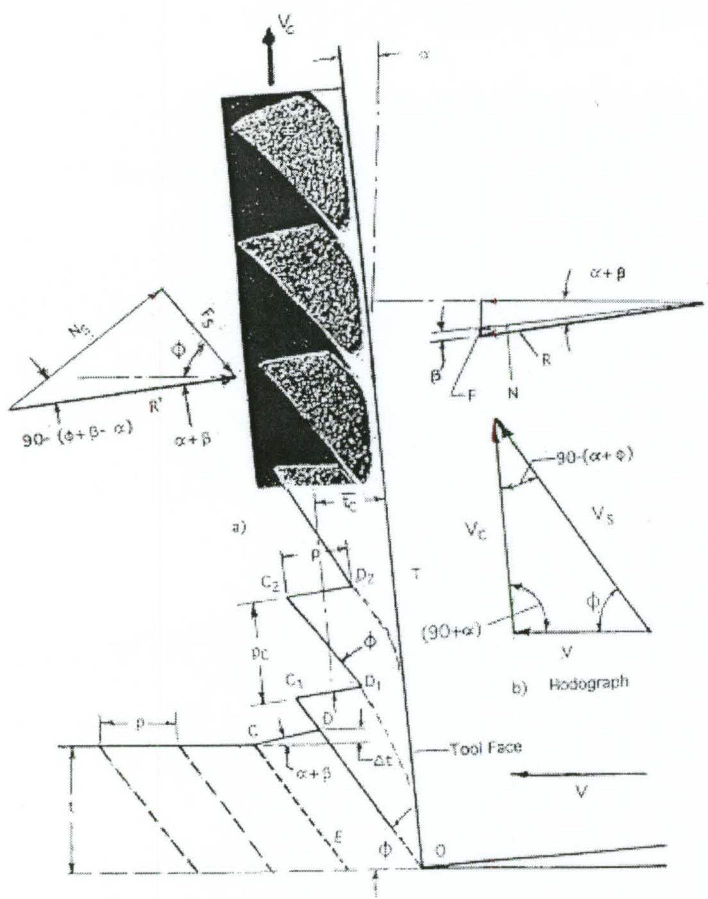

Figure 2.5 Free body diagram of the chip (Shaw, 1998).

The cutting ratio r can be calculated using the mean tooth pitch p_C and the mean value of CD (p) such that

$$r = \frac{p_C}{p} = \frac{V_C}{V} \tag{2.25}$$

The cutting ratio is usually greater than one when saw-tooth chips are produced in steel using a zero or negative rake angle tool. The total specific energy u for a saw-tooth chip can be calculated by summing the following terms

$$u = u_{exten} + u_{crack} + u_{GC} + u_F \tag{2.26}$$

where

u_{exten} is the specific energy for upward flow preceding crack formation

u_{crack} is specific energy for crack formation

u_{GC} is the specific energy for the gross cracked region of the chip

u_F is the specific energy associated with friction between the tool and chip

The values of u_{exten} and u_{crack} are negligible in magnitude in comparison with the other specific energy components. Three of these four values can be calculated as

$$u = \frac{[R\cos(\alpha+\beta)V]}{Vbt} = \left(\frac{R}{bt}\right)\cos(\alpha+\beta) \tag{2.27}$$

$$u_{GC} = \frac{\mu_S N_S V}{Vbt} = [\mu_S \cos(\phi+\alpha+\beta)]\left(\frac{V_S}{V}\right)\left(\frac{R'}{bt}\right) \tag{2.28}$$

$$u_F = \left(\frac{R}{bt}\sin\beta\right)\left(\frac{V_C}{V}\right) \tag{2.29}$$

where u_S is the coefficient of sliding friction and is usually estimated as 0.4 for steels (Shaw, 1998). The fourth value can be solved through difference where none of the values can be negative. The cracking frequency can be calculated as

$$CF = \frac{V_C}{p_C} = \frac{rV}{p_C} \tag{2.30}$$

where the frequency generally approaches the upper limit of audible sound. The shear band in the *MC* region contains highly localized inhomogeneous strain under high compressive pressure. In this region, micro cracks propagate in the shear plane direction but voids are repressed due to high normal forces and compressive pressure. A process such as twinning could occur within this region. Only this band shows evidence of adiabatic shear. The temperature generated in this shear band due to deformation often exceeds the transformation temperature of ferrite (α iron) to austenite (γ iron). The austenite phase at high temperatures is known to be soft and easily deformable. These quickly cooled white regions left after chip formation have been identified as untempered Martensite. This high temperature γ phase is also found on the rake face of the tool and is the reason why the values of u_F and u_{MC} tend to be lower as the chips become more segmented with increases in cutting speed (Shaw, 1998).

2.2.2 Thermo-Mechanical Shear Instability Model

This thermo mechanical shear instability model was pioneered by Recht (1964) when he proposed that saw-tooth chip formation was due to adiabatic shear localization. Adiabatic shear is defined as the point at which thermal softening dominates over dynamic hardening. This is described on a true stress strain curve by the point where the instantaneous plastic modulus E_p has a siope of zero. In high speed machining processes, the strain rate is so high and the gradient of strain is so low such that all the heat generated is localized and has no time to be conducted away from its source. High speed machining processes can generally be assumed to be adiabatic in nature due to the fact that thermal conduction does not have enough time to affect the temperature in the region of the chip formation process. Recht formulated a equation to predict the onset of catastrophic slip in the primary shear zone based on the thermo physical properties of the material such that

$$0 \le \frac{\partial \tau / \partial \varepsilon}{\partial \tau / \partial \theta \left(\partial \theta / \partial \varepsilon \right)} \le 1.0 \qquad (2.31)$$

where τ, ε, θ, are the shear stress, shear strain, and temperature respectively (Komanduri, 1997). According to this equation, catastrophic shear will be imminent when the ratio is equal to 1 and will occur between the values of 0 and 1. When the value is greater than 1, the workpiece material strain hardens more than it thermally softens. Figure 2.6(a)-(c) shows different stages of the chip formation as outlined by the shear localized model.

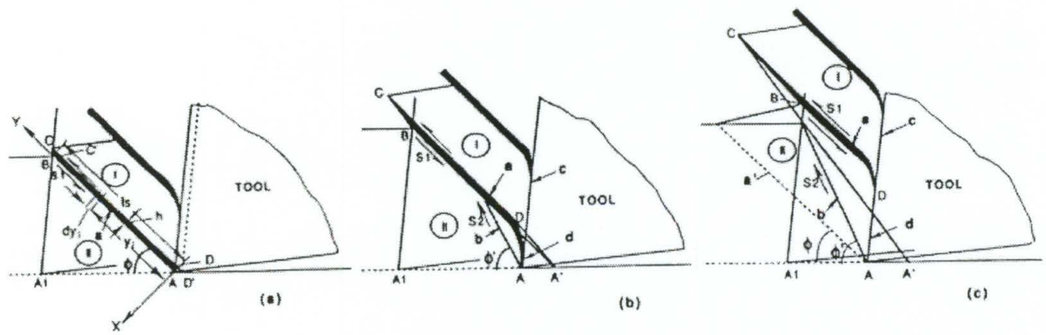

Figure 2.6 Schematic of the different stages of shear localization in machining showing the multiple heat sources contributing to the temperature increase in the shear band (Komanduri and Hou, 1997).

Figure 2.6(a) shows the initial stage of chip formation when a segment I has just been formed and shear *S1* begins on the weakest plane *a*. This intense shear zone is bordered by *ABCD*. Figure 2.6(b) shows the next major stage of chip formation where the shear band has widened from *AB* (figure 2.6(a)) to *A'C* (figure 2.6(b)) and has rotated slightly due to the upsetting of the chip. Segment *S2* begins to deform due to the tool movement and this shear is localized in shear plane *b*. As the chip is upwardly extruded along the rake face, intense frictional shear occurs on the rake face and between the formed segment and the unformed workpiece segment. The heat source on the rake face due to secondary frictional shear is represented by *d* in figure 2.6. Figure 2.6(c) shows the final stage of chip formation where the heat generation in *d* reaches a maximum and the weakest plane of deformation shifts to a' (Komanduri and Hou, 1997).

Temperature increase in cyclic chip formation can be attributed to the plastic work that creates four separate heat sources as shown in figure 2.6. The first is the heat-source *a* due to the primary shear band of intense shear between the separate segments. This source tends to be the dominant one when high cutting speeds and feeds are involved in the cutting operation. The secondary shear heat source *b* is formed during the upsetting stage of chip formation. The third heat source *c* is due to the friction between the segment already formed and the rake face of the tool. The fourth heat source *d* is due to the intense frictional shear between the segment just formed and the rake face during the final upsetting stage of chip formation. This heat source *d* is the second largest heat source only after the primary heat source *a*.

The heat sources are modeled using Jaeger's (1943) classical solution for instantaneous line heat sources. The temperatures calculated are used to resolve the shear stress of the material in the shear band. If the shear stress of the material in the shear band is more than the shear strength of the original or surrounding material, a localized instability occurs and segmentation becomes imminent. Figure 2.7 shows the variation of shear stress σ' in the shear band at the shear band temperature and the shear strength of the original material σ at the preheating temperature with respect to cutting speed V for AISI 4340 alloy steel.

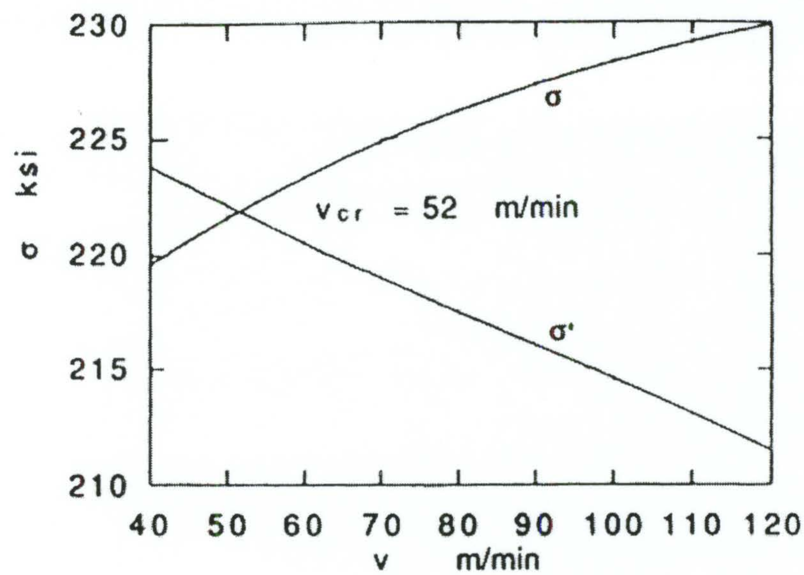

Figure 2.7 Variation of shear stress in the shear band, σ' at the shear band temperature and shear strength of the bulk material at the preheating temperature, σ with respect to the cutting speed in the orthogonal machining of AISI 4340 steel (Komanduri and Hou, 1997).

When σ' is greater than or equal to σ, strain hardening predominates and chip formation is continuous. If σ is greater than σ', thermal softening is dominant and localized instability leading to segmented chip formation occurs. Chip segmentation was calculated to occur at the intersection point of the two curves with a cutting speed above 52 m/min. This result was in good agreement with the experimental observation of segmentation at a cutting speed of 60 m/min (Komanduri and Hou, 1997).

CHAPTER 3

FINITE ELEMENT THEORY AND APPLICATIONS TO MACHINING PROCESSES

3.1 Finite Element Methods and Theory

Traditional finite element techniques applied to linear and non-linear static problems have been based on direct methods. In order to resolve linear systems using direct methods, large numbers of equilibrium equations are formed and must be solved using direct solvers such as frontal, skyline, or Cholesky-type methods. When non-linearities exist, equilibrium iterations must be performed using Newton-Raphson or quasi-Newton methods in order to resolve the system at subsequent load steps. When the problem includes complex geometry, large deformation, large local element rotations, extensive sliding contact surfaces, and highly non-linear material properties, direct methods are so computationally expensive that solutions become impossible. These shortcomings are even more apparent in the case of highly non-linear transient problems such as metal cutting where direct methods will fall dramatically short of a solution.

Explicit methods offer a solution to highly non-linear transient problems such as metal cutting by avoiding massive internal memory requirements and the need to form, invert, and solve a global stiffness matrix inherent to direct methods. Explicit methods are particularly advantageous in computational mechanics due to the fact that all quantities are treated as vectors. The advantages in computational expense of explicit methods are high as the numbers of degrees of freedom increases the size of the numerical problem increases only proportionally. This allows for solutions to problems involving tens of thousands of degrees of freedom. Figure 3.1.1 shows a comparison of the number of operations with respect to the number of elements for direct and explicit methods. Figure 3.1.2 shows a comparison of the memory requirements for transient analysis inherent to both methods. The advantages of explicit methods are quite apparent as the number of elements is increased within a problem. Robust contact algorithms can also be implemented in explicit methods due to the fact that changes in model connectivity are not an issue with this type of solution.

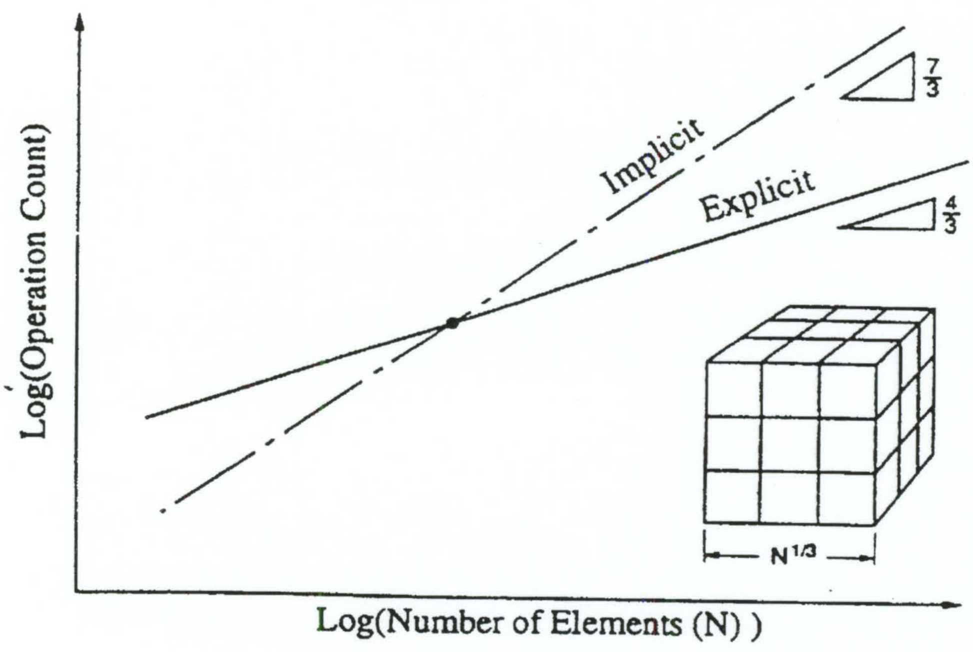

Figure 3.1.1 Comparison of operation count for nonlinear transient analysis (Sauvé and Metzger, 1995).

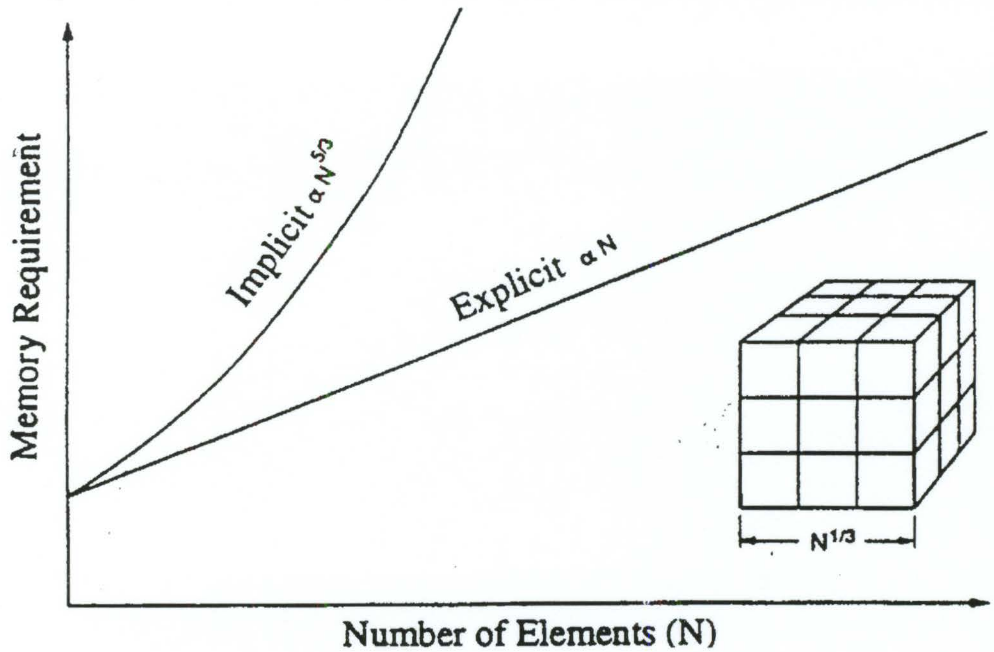

Figure 3.1.2 Comparison of memory requirements for nonlinear transient analysis (Sauvé and Metzger, 1995).

3.1.1 Explicit Methods

The central difference operator is used to perform time integration on the discretized equations of motion given by

$$M\ddot{x} = F_{ext}^{t} - F_{\text{int}}^{t} \qquad (3.1.1)$$

where M is the mass matrix, F_{int}^{t} and F_{ext}^{t} are the element internal and external forces vectors respectively. The F_{int}^{t} internal force vector is defined by

$$F_{\text{int}}^{t} = \int_{V} B^{T} \sigma dV \qquad (3.1.2)$$

where B is the gradient interpolating matrix relating element nodal velocities to element velocity strains. Figure 3.1.3 shows the general format of the central difference operator and how accelerations, velocities, and positions are updated every time step. Using the explicit integration method, discretized accelerations $\ddot{x}$, velocities $\dot{x}$, and positions x are known at time t. In order to advance a time step and know what these quantities are at the new time $t+\Delta t$, where Δt is a time step dependant on the Courant stability limit. In order to calculate the quantities at the new time $t+\Delta t$, half step approximation is used and the new constant velocity over that step is found as

$$\dot{x}^{t+\Delta t/2} = \dot{x}^{t-\Delta t/2} + \Delta t \ddot{x}^{t} \qquad (3.1.3)$$

and the new position at $t+\Delta t$ is calculated using this velocity and is given by

$$x^{x+\Delta t} = x^{t} + \Delta t \dot{x}^{t+\Delta t/2} \qquad (3.1.4)$$

using the current calculated geometry, the stresses are calculated using the appropriate constitutive laws.

The temporal integration scheme described is explicit in that dynamic equilibrium is satisfied at time t. The unknown velocities and positions at time $t+\Delta t/2$ are defined in terms of the known velocities and positions calculated and applied for the previous time step. At each time step, all constitutive calculations and element geometry are evaluated and updated for the new geometry at time $t+\Delta t/2$. Using a lumped mass matrix M, the need to form a banded system stiffness matrix and solution is avoided. The explicit method is conditionally stable such that the critical time step is based on the Courant stability limit where

$$\Delta t \leq \frac{2}{\omega_{max}} \qquad (3.1.5)$$

and where ω_{max} is the highest frequency in the system. In this case, stability is only possible when the time step is smaller than the time that it takes for an elastic or acoustic wave to travel the shortest distance across the smallest discrete element distance in the entire system. The central difference operator is outlined in figure 3.1.3. The entire explicit computational cycle for a non-linear transient problem is shown in figure 3.1.4 (Sauvé and Metzger, 1995).

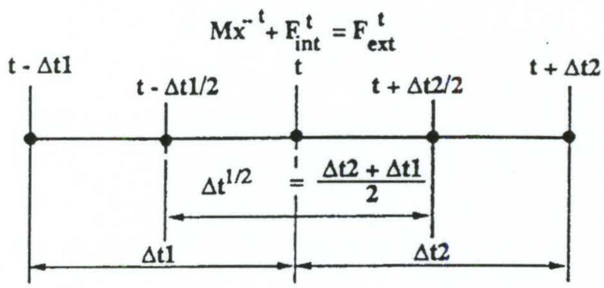

- $\ddot{x}^t = M^{-1} [F^t_{ext} - F^t_{int}]$ **(Acceleration)**
- $\dot{x}^{t+\Delta t2/2} = \dot{x}^{t-\Delta t1/2} + \Delta t^{1/2}\ \ddot{x}^t$ **(Velocity)**
- $x^{t+\Delta t2} = x^t + \Delta t2\ \dot{x}^{t+\Delta t2/2}$ **(Coordinates)**
- **Update Time t + Δt2**
- **Obtain F^t_{int} and Repeat**

Stability governed by Courant Condition

Figure 3.1.3 The central difference operator computational cycle (Sauvé and Metzger, 1995).

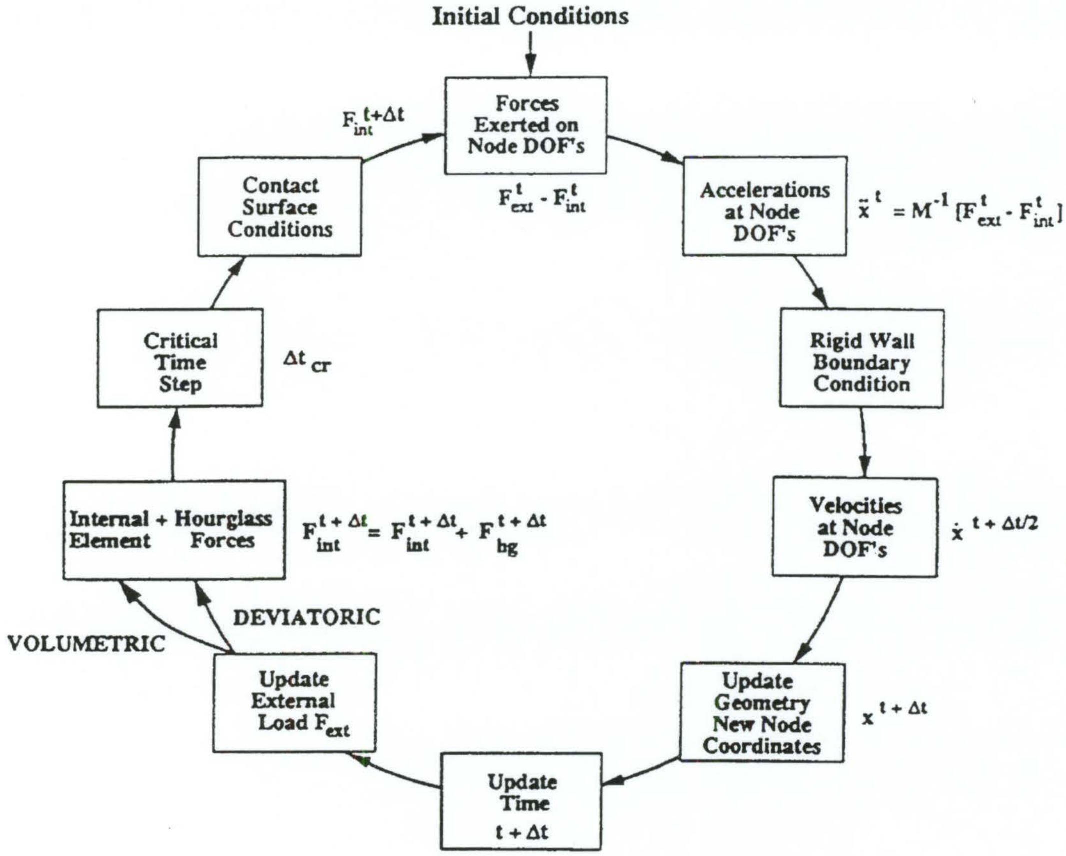

Figure 3.1.4 The explicit non-linear transient computational cycle (Sauvé and Metzger, 1995).

3.1.2 The Contact Algorithm

The penalty method is used in this solution algorithm to treat contact between separate colliding bodies. Surfaces are assigned as either master of slave surfaces for a set of defined contact conditions. The slave surfaces are made up of four nodes and contact is treated in terms of slave node penetration into a corresponding master contact surface.

The master surface is also made up of four nodes but is treated as a surface defined by these points. Should any slave node penetrate the master surface, a force in a direction normal to the surface is applied to the slave node such that the slave node is pushed out of the surface.

This force is also used to calculate the imposed friction force tangential to the master surface according to the appropriate friction model. The normal force applied is proportional to the penetration distance and is a function of the master surface area and material properties. Contact damping is applied to this algorithm and is used for the purposes of this work in order to smooth the acceleration gradient over time experienced by a penetrating slave node. An element can go super plastic within a few time steps should a node attached to it move too quickly. Hence the solution stability of the explicit method was not undermined by using this technique for treating contact.

3.2 Finite Element Models of Machining Processes

A literature review of current published works in the field of finite element modeling of metal cutting operations were reviewed in order to compare differing results, assumptions, and approaches to this complex problem. Most of the works dealt with 2-D orthogonal plane-strain modeling, while some works managed to compare continuous and discontinuous chip formation with experimental results.

Considerable work has been published in the last twenty years on the simulation of orthogonal machining using finite element techniques. While much work has been done, few of these simulations have managed to produce relevant results due to the complexity of the machining process. Highly non-linear plastic deformation, friction between the chip and rake face, and chip separation mechanisms are the main mechanical aspects of concern. The friction forces and plastic work encountered during chip formation also generates heat, which then in turn affects the material properties. This heat is then transferred in part to the chip as well as the tool until a steady state is reached. Hence, only a thermo-mechanical simulation can begin to fully model a metal cutting operation.

The lack of material data for conditions encountered in metal cutting has hindered the progress of realistic simulation. High temperatures, strain rates, pressures, and complex fracture mechanics are some of the variables that must be considered in detail. While many of these issues have been examined in the simulation of continuous chip formation, adiabatic shear localization, damage, and fracture thought to be present in discontinuous chip formation have yet to be fully addressed. Reviews of the most detailed and relevant published results to date are included within this work.

3.2.1 Literature Review

Obikawa and Sasahara (1997) published a detailed work on a simulation of discontinuous chip formation at low cutting speeds. This paper used an updated lagrangian approach, which allows for large element deformation. Using a 2-D orthogonal plane-strain idealisation, an elasto-plastic approach, and ductile fracture criterion for crack growth, discontinuous chip formation was modeled and compared with experimental results. Three different types of brass were modeled in this simulation. Temperature was ignored, which resulted in the neglect of the heating effects on the flow stress of the material. Stress-strain curves were obtained using uniaxial compression test data at a low strain rate of $10^{-3}s^{-1}$. Hence, this model can only be applicable in validity at extremely low cutting speeds. This limits the model, making it only useful in the understanding of the mechanics of discontinuous chip formation without the influence of strain rate and temperature. The tool was rigid in this model, and thus, the tool's dynamic influence on the process was not considered. Four noded quadrilateral isoparametric elements with constant dilation were used, and were arranged in the mesh as shown in figure 3.2.1.

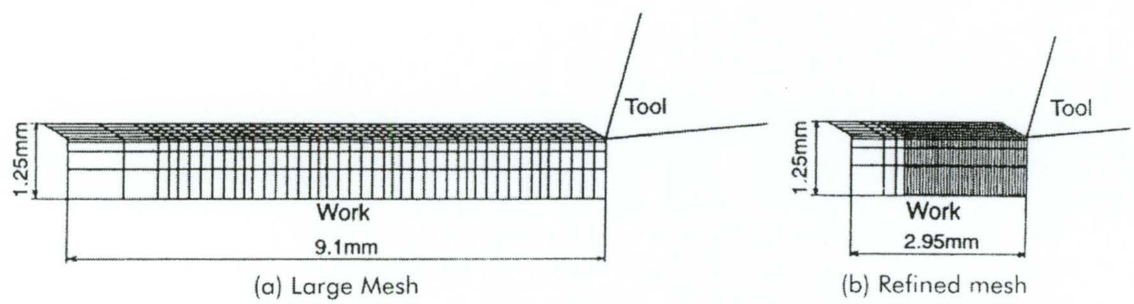

Figure 3.2.1. A coarse and a refined workpiece mesh (Obikawa and Sasahara, 1997).

The friction condition on the rake face was defined in terms of normal stress σ_N and frictional work ω'_f (equation 3.2.1). When the normal stress is compressive and the frictional work is positive, the node slides. When the normal stress is compressive, but the frictional work is equal to zero, the node sticks, and thus static friction is induced. The contact length is defined by separation when the normal stress is equal to zero and the rate of normal stress is negative. The characteristic constant of friction C was defined experimentally as approximately equal to one. τ_f is the frictional stress and τ_e is the shear flow stress of the strained chip (Obikawa and Sasahara, 1997).

$$\frac{\tau_f}{\tau_e} = 1 - \exp\left(-C\frac{\sigma_N}{\tau_e}\right) \qquad (3.2.1)$$

The node separation criterion used in this model was a geometric one. The distance from the tool tip at which separation would occur was defined as 5μm (1/50 the undeformed chip thickness). This value was modified, and it was found that the reduction of distance increased the residual stresses in the finished surface. This criterion was a functional but weak one, for it was not based on physical or material process and was arrived at though trial and error.

The fracture criterion defined in this model was based on an equivalent plastic strain criterion. When the equivalent plastic strain exceeded the fracture strain of the material, fracture occurred. The fracture strain of the material was based on hydrostatic pressure ρ, the plastic strain rate $\dot{\varepsilon}^P$, the cutting speed V_C, equivalent stress σ, and experimentally determined constants ε_O, α, and β (Obikawa and Sasahara, 1997). As ρ or the $\dot{\varepsilon}^P$ went up, the critical fracture strain ε_C went down as shown in equation 3.2.2.

$$\varepsilon_C = \varepsilon_O - \alpha\frac{\rho}{\sigma} - \beta\frac{\dot{\varepsilon}^P}{V_C} \qquad (3.2.2)$$

The crack growth and direction are defined by the separation criterion as explained in chapter 3.3. It was assumed that the chips on both sides of the nominal crack could slide mutually without friction and parallel to the actual crack. Friction should have been introduced along these slide lines in this model, but were neglected due to low speed and oversimplification of the model. The comparison of the computed results with experiment were good in this model, where chip shape in continuous and discontinuous states as well as cutting forces were compared. This paper was unique in forming a definite link between residual stresses on the finished surface and the nodal separation criterion of the model.

Zhang and Bagchi (1994) presented a model that used a 2-D orthogonal plane-strain idealisation to simulate the formation of a continuous chip from 70/30 Brass. Low speed and temperatures were used, and hence, the strain rate and temperature effects were neglected in this model. This leads to very limited applicability to metal cutting operations, and hence the simulation was assessed as a tool used to further our understanding of the processes at work. . The mapping of the hardness profile of the deformed chip was an interesting tool for the analysis of the simulation. This model was unique in its use of true stress-strain curves for the material where the data at higher strain rates was interpolated (figure 3.2.2).

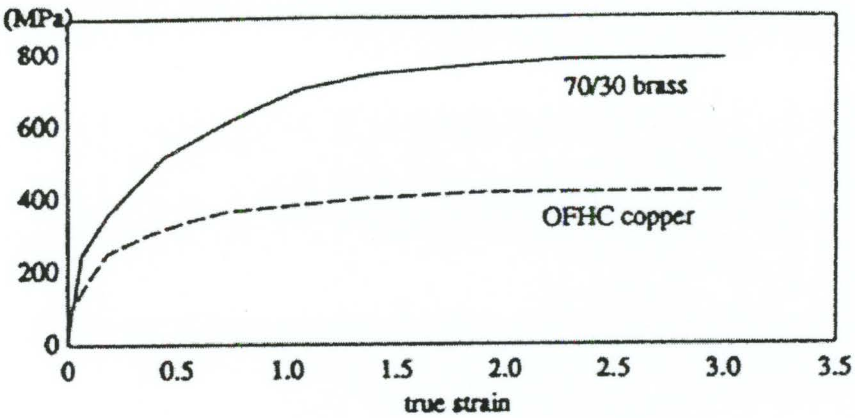

Figure 3.2.2 True stress-strain curves (Zhang and Bagchi, 1994).

The chip separation criterion used in this model was a geometric one, where the distance from the tool tip chosen between (.1 to .3)* *l*, where *l* was the side length of the solid element. The generation of two new surfaces was achieved by using two noded conditional link elements to link the two surfaces along a predefined line of separation. The fact that the line of separation was predefined limited this model to simple continuous chip formation. Thus this model had poor and idealized separation criteria. The element mesh consisted of 264 linear isoparametric quadrilateral elements, with the highest density near the tool where deformation was the largest. 37 interface elements were used to simulate the tool chip interface interaction, and 34 conditional link elements were used to join the two surfaces (figure 3.2.3).

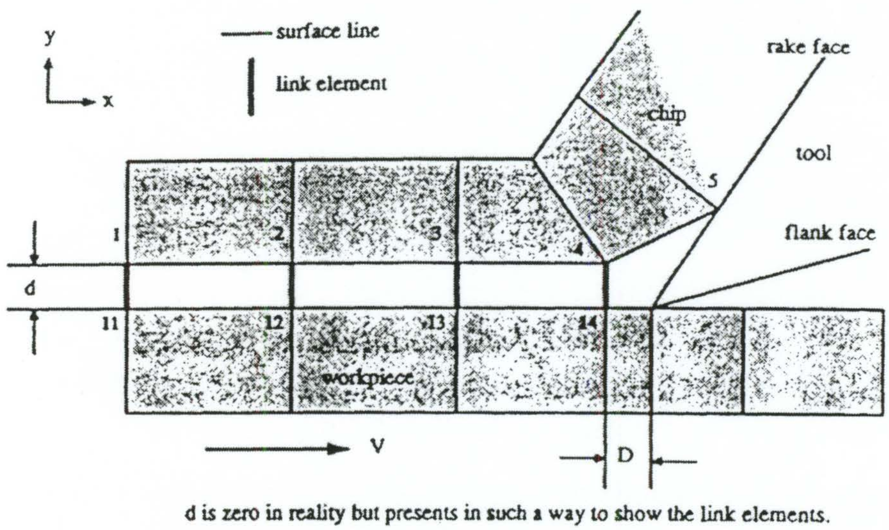

Figure 3.2.3 Illustration of conditional link elements in the model (Zhang and Bagchi, 1994).

The friction condition on the rake face for this model was again a stick slip condition as explained in chapter 3.3. Whenever the nodes contacted the rake face, normal stress was calculated from the strain in the deformed body. The coefficient of friction was determined experimentally from the stress distribution on the rake face, but was difficult to determine by other means due to strain hardening and new surface generation. The maximum shear strength of the chip was used as a limit on the frictional forces in order to simulate the sliding and sticking phenomena. The compared results agreed well with the experimental mean coefficient of friction.

The comparison of computed results to experimental data from literature was unique in concept, but it was found the materials compared were actually different. The results of the comparison were very questionable due to this discrepancy. This model was unique in its different approach to determine the angle of the shear plane, where an empirical relation was used as well as a determination through the examination of the plastic strain contours of the model results. The compared results were good using the two methods. This model also created a hardness map of a chip using the relation curve between plastic strain and hardness.

Shirakashi and Maekawa (1996) presented a paper that described recent progress in the FEM process applied to metal machining. A comprehensive explanation of the basics of FEM formulation was provided, applied to continuum mechanics for large deformation problems. These were the only authors that addressed tool damage characteristics. This work covered a more computationally efficient scheme for the updated lagrangian process. While the iteration loop needs an initial chip shape to be defined apriori, this loop actually recalculated the shape the chip by iterations that developed loads in the chip and tool. A plastic state then developed and was checked to see if it was consistent with the assumed chip shape. If not, the chip was systematically altered and the calculation was repeated. This finite element method used time stepping and hence was able to take heat generation, temperature rise, and flow properties into consideration. Consequently, work hardening and work softening were introduced into the model. The distribution of equivalent plàstic strain rate and the temperature isotherms resulting from this model both appear to be within realistic bounds.

This paper (Shirakashi and Maekawa, 1996) also referred to a three-dimensional finite element simulation created by Sasahara, Obikawa, and Shirakashi (1994). This model used the iterative convergence scheme to simulate a continuous chip formation process. The 3-D dynamic effect of the tool was taken into consideration in this model. Figure 3.2.4 shows the element deformation of the workpiece as the tool begins the cut. Figure 3.2.5 shows the equivalent plastic strain for the same situation. The residual strain generated by the front cutting edge was found to be greater than the strain created by the side-cutting surface.

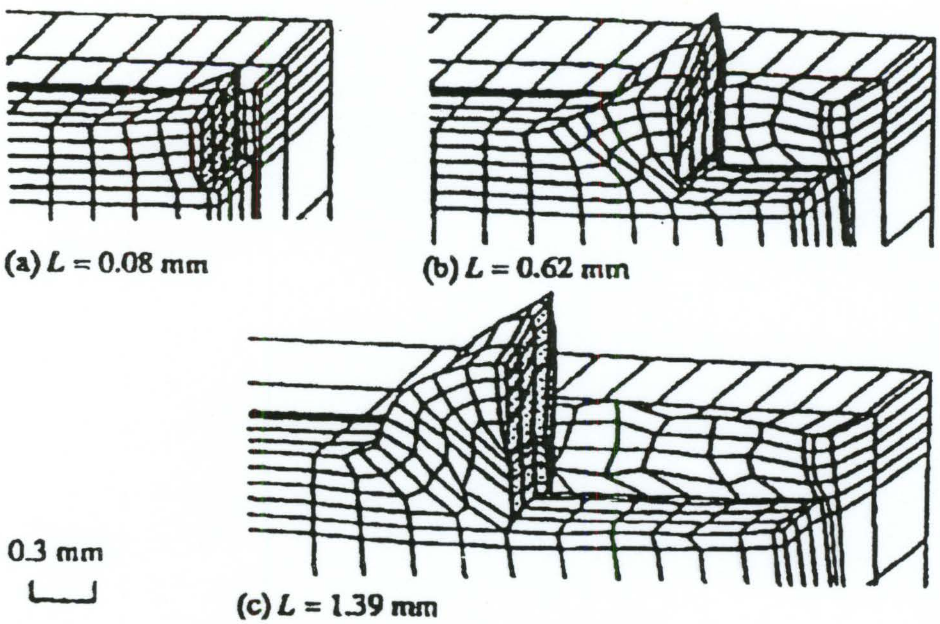

Figure 3.2.4 Predicted deformation field upon tool entry (Sasahara, Obikawa, and Shirakashi, 1994).

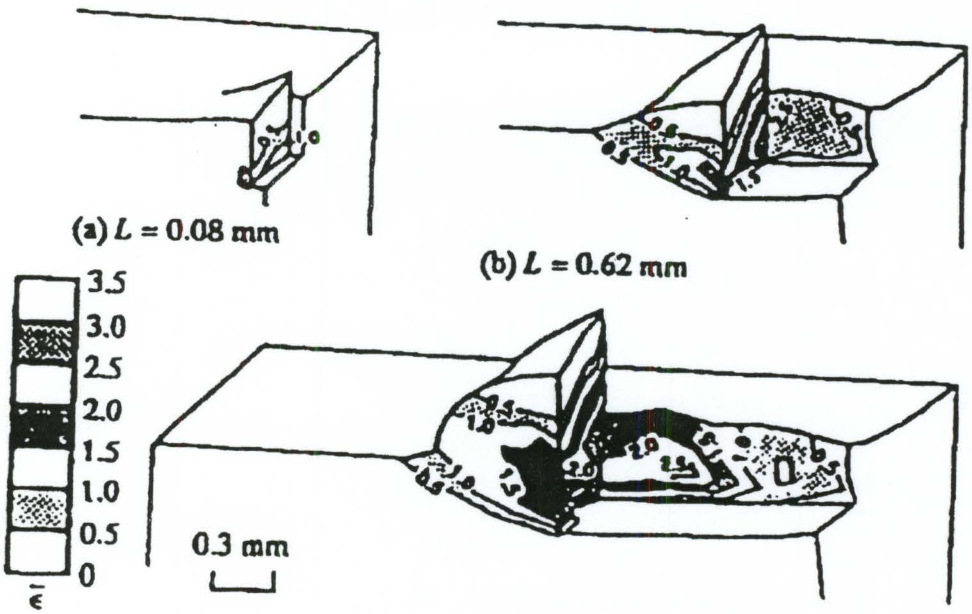

Figure 3.2.5 Distributions of effective plastic strain entry (Sasahara, Obikawa, and Shirakashi, 1994).

Obikawa and Usui (Obikawa and Usui, 1996) presented a work that examined the application of FEA to the machining of titanium alloy modeling a 2-D orthogonal plain-strain process. The finite element mesh was made up of 4 noded quadrilateral isoparametric elements and the tool was assumed to be rigid. This model used an updated lagrangian formulation that took heat generation, and hence, varying material properties into account. The friction condition on the chip tool interface was defined as stick slip and was numerically treated as outlined by Obikawa and Sasahara (1997). The flow stress of the titanium material was obtained from a high temperature and strain rate test performed by the authors. The separation criterion used in this model was geometric. The crack initiation and fracture propagation criterion applied were also the same as those outlined by Obikawa and Sasahara (1997) and provided insight into fracture criterion for crack initiation and propagation.

The results exhibited the adiabatic chip formation process in titanium machining well. The plastic strains were concentrated between the crack tips and the tool face as shown in figure 3.2.6. The cutting forces calculated resemble the experimental results and the temperature isotherms (figure 3.2.7) exhibited expected high temperatures encountered in the machining of titanium.

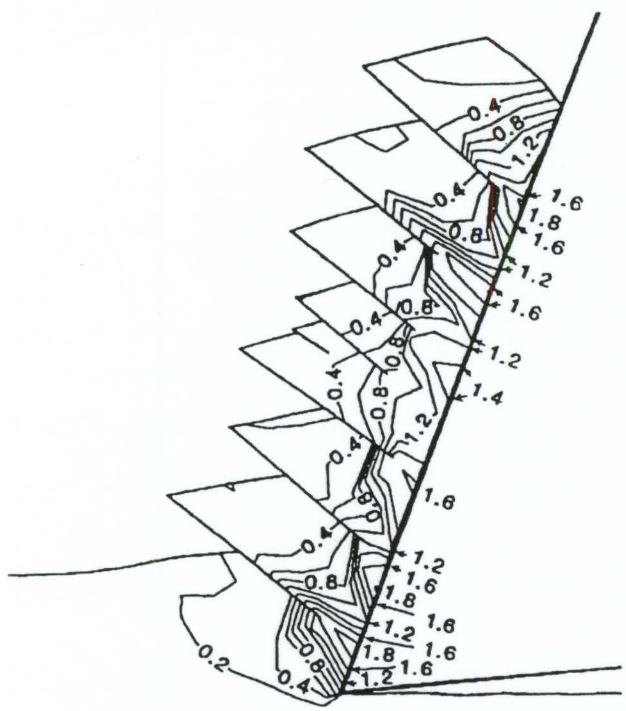

Figure 3.2.6 Distribution of equivalent plastic strain at Vs = .5m/s (Obikawa and Sasahara, 1997).

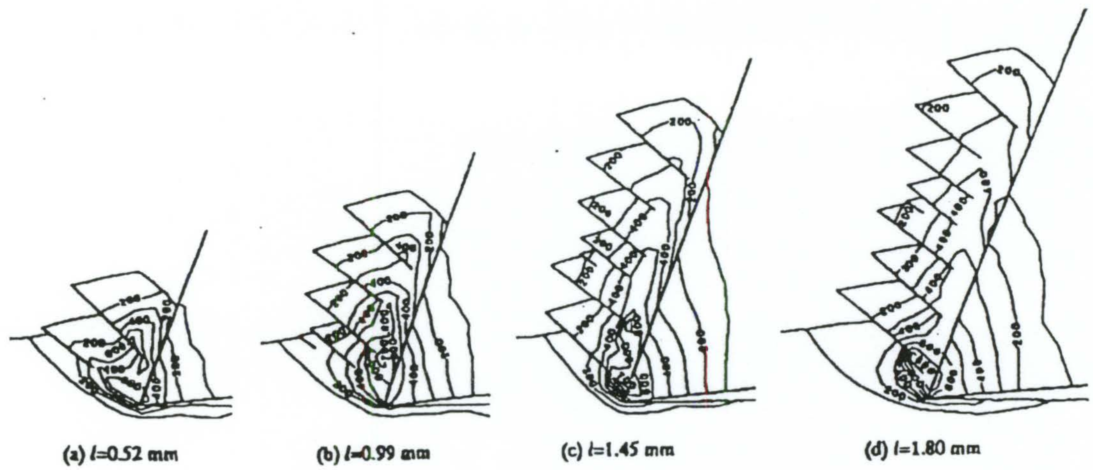

Figure 3.2.7 Temperature distributions at Vs = .5m/s s (Obikawa and Sasahara, 1997).

Meir and Hashemi (1988) presented a work that simulated segmented chip formation in high speed machining. A program called DEFEL (Dyna East Finite Element Lagrangian) was used to simulate an elasto-plastic 2-D orthogonal plane-strain problem. This program took into account large strain, thermal, work hardening, and strain rate effects. It was unique in its ability to simulate friction along newly formed fracture surfaces by introducing slide lines along free boundaries. It used three noded triangular elements with mass lumped at the nodes. When a node was split, the mass was divided proportionally into the two nodes dependant on the number of elements attached to each of the elements concerned.

Four different separation criterions were attempted, not including a geometric criterion. It was found that a maximum effective plastic strain criterion functioned the most realistically. At low speeds, continuous chips were formed, and at high speeds, discontinuous chips were formed. Upon the branching of a crack, a previously split node was split again, and slide lines were inserted at the branching point. This was a good example of how slide lines can be inserted and deleted between newly created surfaces. The use of three noded constant stress triangular elements was very limiting. These elements have a very poor spectral response and are well known to shear lock. While the deformation results may look good, the order of stress error in a model using these elements is very poor and is quite inaccurate and misleading.

Strenkowski and Carroll (1985) produced a work using a program called NIKE2D to simulate 2-D elasto-plastic orthogonal continuous chip formation. This model was incapable of modeling discontinuous chip formation. 820 linear isoparametric quadrilateral elements were used to model the machining of 2024-T4-aluminium alloy. The program used an incremental equilibrium equation to resolve the forces, and it updated the stiffness matrix to the latest geometry if the solution did not converge. An effective strain criterion was used to model node separation and new surface generation. This simulation was limited in its ability to produce segmented chips as slide lines had to be predefined. Heat per unit volume was generated in the chip and workpiece and was expressed in terms of plastic work. The heat generation term was then related to the material density and specific heat, effectively modeling adiabatic heating within each element. The residual stresses in the finished surface were also calculated, but the results were not compared with experiment.

Marusich and Ortiz (1995) presented the most comprehensive model describing both continuous and discontinuous chip formation in low and high speed machining applications. This model included adaptive remeshing techniques, brittle and ductile fracture criteria, friction, and thermo-mechanical coupling. A large strain Lagrangian algorithm based on elasto-plastic multiplicative decomposition and the explicit time integration scheme was employed. A Von-Mises based yield criterion was used and the material model considered strain hardening, strain rate, and linear thermal softening. Coulomb's law was used to model friction and the tool was assumed rigid. The thermal analysis was based on a staggered calculation procedure. Fracture was modeled using both brittle and ductile fracture criteria. Brittle fracture was based on the fracture toughness model, where σ_f is the critical fracture stress, K_{IC} is the toughness, and l is the spacing between grain boundary carbides, typically on the order of two grain diameters (equation 3.2.3). Ductile fracture was based on a simplified Rice and Tracey criterion (equation 3.2.4) where ε_f^p is the critical effective plastic strain, ρ is the pressure, and $\bar{\sigma}$ is the effective Von Mises stress.

$$\sigma_f = \frac{K_{IC}}{\sqrt{2\pi l}} \qquad (3.2.3)$$

$$\varepsilon_f^p \approx 2.48e^{-1.5\rho/\bar{\sigma}} \qquad (3.2.4)$$

The adaptive meshing procedure used plastic work rate as a refinement indicator. This was the first FEA of machining that was used to predict the cutting speed transition from continuous to segmented chip formation.

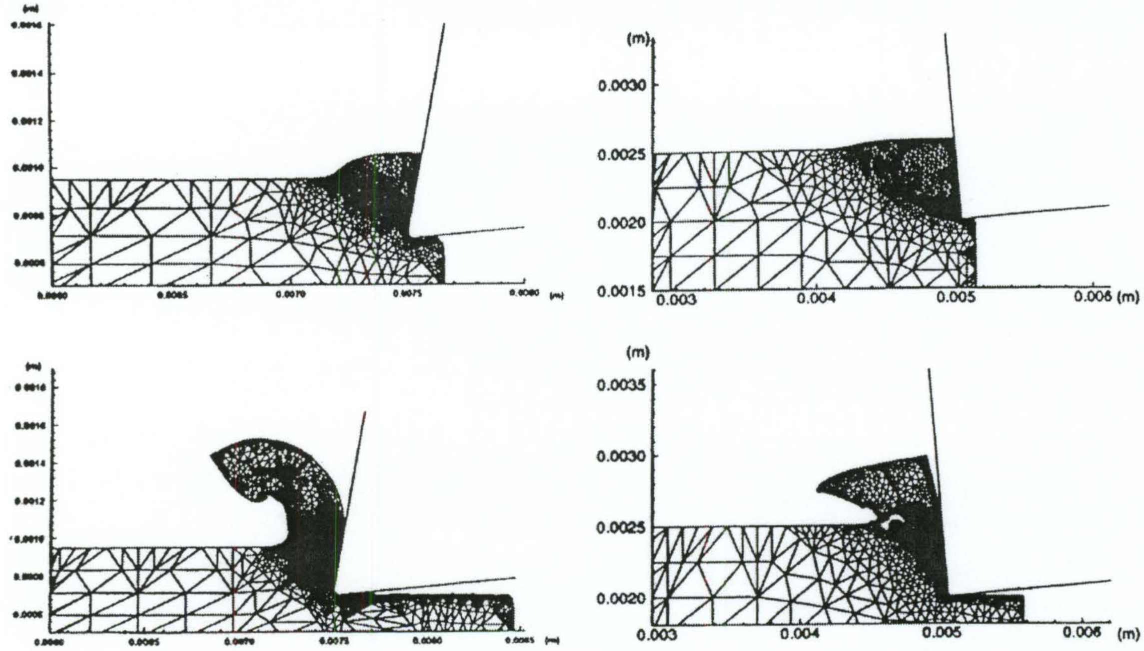

Figure 3.2.8 Chip formation in AISI 4340 (a) Continuous chip formation at Vs = 30 m/sec, Rake = 10 deg. (b) Discontinuous chip formation at Vs = 10m/sec, Rake = -5 deg. (Marusich and Ortiz, 1995)

3.2.1 Conclusions

Each of the different these models have their strengths and weaknesses. The work by Obikawa and Sasahara (1997) was a good tool for understanding the mechanisms at work in discontinuous chip formation, but it neglected temperature and strain rate effects and was not applicable to high-speed operations. The comparison between computation and experiment was performed well and the results are well justified within the speed range modeled.

The work by Zhang and Bagchi (1994) was again a good tool in understanding the mechanics of continuous chip formation. It did use true stress-strain curves in a high true strain rate, but again, its low speed idealisation ignored temperature and strain rate effects. The mapping of the hardness profile of the deformed chip was a unique intuitive tool in the analysis of the work. The work by Maekawa and Shirakashi was an excellent paper that explained the processes of the FEM analysis and that took temperature and strain rate effects into account by using a time-stepping algorithm. A simple 3-D model was introduced in this work, but the data provided was only for tool entry into an elasto-perfectly-plastic material.

The work by Obikawa and Sasahara (1997) included a model that took heat generation with adiabatic conditions into account. This model was useful in providing insight into fracture criterion for crack initiation and propagation. The work by Meir and Hashemi (1988) was strong in the fact that it provided a provision for friction forces between newly formed fracture surfaces. The creation of two nodes from a single node involved assigning the same velocity and position to the new nodes. The mass of each new node was assigned based on the proportion of associated element volume, and hence, momentum was preserved at that point. The work by Strenkowski and Carroll (1985) provided excellent separation criterion for new surface generation as well as a good heat generation procedure within the elements. It was limited in its ability to produce segmented chips and weak because the slide lines had to be defined a-priori.

The work by Marusich and Ortiz (1995) was the most comprehensive and accurate work encountered by the author. The replication, verification, and extension of this work were the primary objectives of the author as the results presented are the most realistic in the field of the simulation of high-speed discontinuous chip formation. The work presented in this publication is the fundamental foundation for a commercial machining simulation software called 3rd Wave Systems released to the market in 1998 by T.D Marusich.

3.3 Numerical Modeling of Mechanical Processes Involved in Metal Cutting

Metal Cutting operations involve many different non-linear processes. In an attempt to model these processes, they were examined individually and under specific controlled experimental conditions. By coupling experiment with theoretical and numerical modeling, an understanding was established to predict these phenomenons using only explicitly specified boundary conditions. Extreme non-linearity is pronounced in high speed machining operations as these processes are often also coupled. Hence what can conventionally be described under specific conditions are no longer discernable using currently existing experimental machining techniques. By using numerical simulation such as finite element analysis to model experiment, each of these processes can be decoupled and examined in detail.

The processes involved in metal cutting can be separated into thermal, mechanical, and coupled thermo-mechanical processes. The thermal effects in metal cutting operations include the generation of heat due to deformation and friction, the transportation of this heat, and its effects on the structure of the material. Elastic deformation, plastic flow, fracture, friction, and crack propagation make up the mechanical aspects of the problem. In order to model these processes in numerical space, the ability of a finite element solver capable of reproducing these phenomena is paramount. Hence, modern numerical modeling techniques applied to these processes were reviewed and their implementation was discussed.

3.3.1 Friction Conditions

The friction conditions at the chip tool interface are of particular concern in FEM analysis of continuous and discontinuous chip formation. The key issue is the variation of frictional and normal stress on the rake face. Some finite element models assume that frictional and normal forces are constant along the rake face. This is an inaccurate interpretation, and while mean cutting force results may be realistic, the shape of the deformed chip, the secondary zone of plastic deformation, and the residual stresses left in the workpiece will be far from accurate. The error introduced due to this idealization is more pronounced in the modeling of continuous chip formation. The results will also produce poor temperature and plastic deformation distributions. It is paramount to model the non-uniform stress distributions on the rake face realistically for cutting operations producing continuous chips (figure 3.3.1).

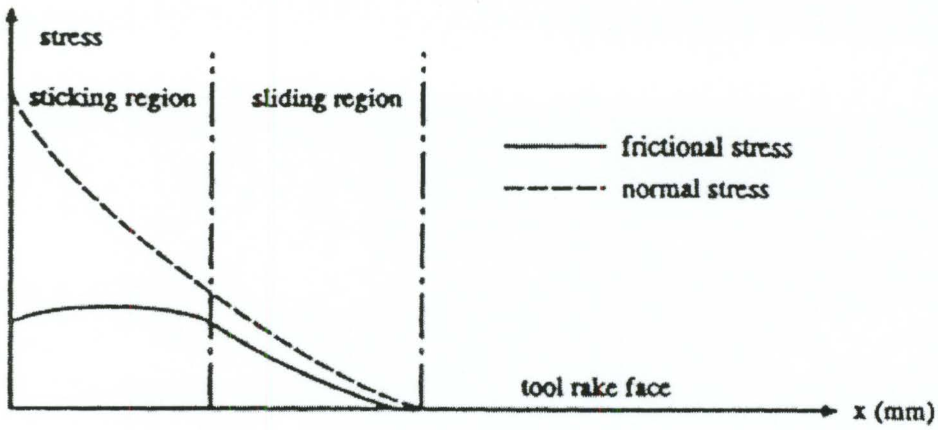

Figure 3.3.1 Generic stress distribution on the rake face of tool (Zhang and Bagchi, 1994).

The rake face is heavily loaded at the tool tip, and lightly loaded where the chip leaves the tool. This means that the friction conditions will vary through two states across the face of the tool, that is, sticking and sliding. In a sliding condition, a constant coefficient of friction can be used, simulating dry friction conditions. In the sticking region, ideal seizure must be modeled, and thus a constant frictional stress is used which is equal to the shear flow stress of the chip material under appropriate temperature and hardness conditions. The coefficient of friction in the sliding region is difficult to determine due to new surface generation and strain hardening of the chip material. Some models have used an incremental analysis with an initial friction coefficient to determine the mean coefficient across the tool face (Shirakashi and Maekawa, 1996). A more realistic interpretation of sticking or sliding criterion is:

$$\tau(x) = \mu\sigma(x) \quad when \quad \tau < \tau' \quad \textit{(Sliding Condition)} \qquad (3.3.1)$$

$$\tau(x) = \tau' \quad when \quad \tau \geq \tau' \quad \textit{(Sticking Condition)} \qquad (3.3.2)$$

Where σ and τ are normal and frictional stresses respectively, μ is the coefficient of friction, and τ' is the shear flow stress of the chip material (Zhang and Bagchi, 1994). Many models use a criterion similar to this generalized one. High-speed cutting operations producing discontinuous chips involve negligible plastic strain in the secondary deformation zone (Komanduri and Schroeder, 1982). Due to this experimental observation, it is safe to assume that a variation in the friction conditions between the rake face and segmenting chip will have a less dramatic effect on the chip morphology in comparison with the modeling of continuous chip formation. This effect was verified as a variation in the modeled friction conditions had little effect of the shape of the segmented chip.

3.3.2 Wear and Brittle Fracture of the Tool

Wear mechanisms such as crater wear and flank wear may be considered within the scheme of a finite element simulation. Wear is a function of temperature, abrasion, diffusion, and fracture. Empirical relations can be incorporated into the FEM analysis by using the varying absolute temperature θ and contact stresses σ_t to approximate the depth wear per unit sliding distance $\partial W/\partial L$ (Shirakashi and Maekawa, 1996).

$$\frac{\partial W}{\partial L} = C_1 \sigma_t \exp\left(-\frac{C_2}{\theta}\right) \qquad (3.2.3)$$

The brittle fracture of a cutting tool can also be empirically estimated. The probability is given by the sum of the probabilities in each element over the tool, where

G_i is the fracture probability of element i and a function of principal stresses, specimen volume, and Weibull's parameters (Shirakashi and Maekawa, 1996).

$$G = 1 - \prod_{i=1}^{n} (1 - G_i) \qquad (3.2.4)$$

Friction due to flank wear may also be considered using an empirical relation that models the coefficient of friction on the flank surface with respect to cutting time. A flat flank land can then be built into the tool mesh geometry, and a time function introducing a variable coefficient of friction on this area can be incorporated.

3.3.3 Finite Element Mesh

Figure 3.3.2 shows two typical kinds of finite element meshes used in computational machining. The large mesh is used where deformations are smaller, and where boundary effects will be minimized. The tight mesh is needed where deformations are large and numerical accuracy and density is needed. An advanced finite element simulation uses a remeshing algorithm to create a tighter mesh of elements in the material approaching a specified distance from the tool. The elements in the undeformed chip region are often skewed in order to reduce the amount of deformation that occurs as the material passes through the shear plane. More comprehensive models incorporate element meshes in the tool in order to take tool dynamics into consideration.

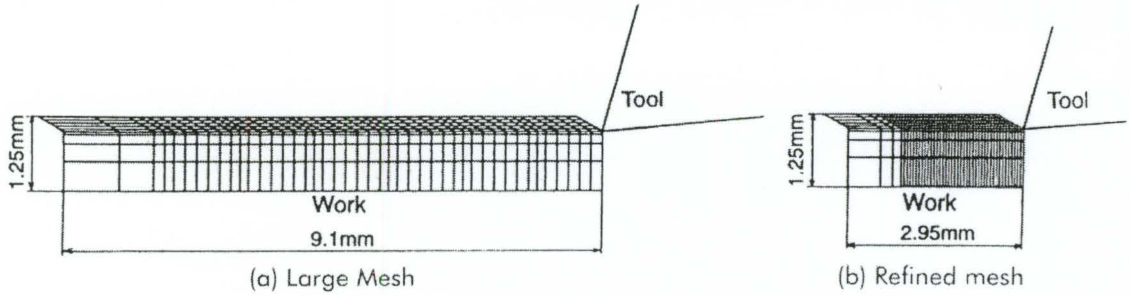

Figure 3.3.2 Finite element meshes (a) a coarse mesh (b) a fine mesh (Obikawa and Sasahara, 1997).

3.3.4 Nodal Separation Criteria and New Surface Generation

As the workpiece material approaches the tool tip, two new surfaces must be generated in order for chip formation to occur. In the FEM process, this involves the separation of connected elements along the tool tip path. Element nodes must be divided or new nodes must be created in order to split the material into the finished workpiece and chip. Separation criterion can be geometric or related to material properties. Maximum normal stress, shearing stress, shearing strain, or effective plastic strain of the material can be used as separation criterion when exceeded at one of the nodes. The geometric separation criterion is satisfied when a node reaches a pre-defined distance from the tool tip and when the previous node is on the rake face of the tool. Creating new nodes or separating nodes can be achieved in many ways. Two noded elements have been used to form a link between elements along a path of separation, hence eliminating the complexities of generating new nodes (Zhang and Bagchi, 1994). Geometric criteria tend to be founded on a weaker argument than material separation criterion. The arbitrary selection of a distance from the tool tip past which separation can occur is often based on trial and error. A material energy related criterion is a more viable representation of the processes at work.

An element erosion method was used within this work in order to model the generation of new surfaces as well as fracture propagation. No works within the extensive literature survey performed by the author contained any reference to this type of method being applied to the simulation of metal cutting. The element erosion principal takes a failed element out of the element internal force calculation of the solution loop. This is performed by slowly reducing the stiffness of a failed element over a number of user defined time steps. This user option introduced by the author for the purposes of this work had a dramatic effect on the stability of the solutions under varying conditions. The work involved in the erosion of an element increases the solution stability of the model by reducing the numerical shock of a sudden loss of volume and stiffness in the overall solution. The criteria used for the determination of a failed element was based on the Rice and Tracey ductile fracture criteria outlined in chapter 4. While this was a functional criterion for the purposes of this work, large inherent disadvantages in the element erosion method reduced the effectiveness of this strain history based criteria as outlined in chapter 5.

3.3.5 Crack Generation and Fracture Propagation in Formation of Discontinuous Chips

Crack generation is a complex process that is highly dependant on temperature, hydrostatic forces, normal and shear forces, direction, and material properties. When the chip begins to pass over the tool tip, high plastic deformation can actually initiate fracture in the chip material, and thus create a discontinuous chip. Crack propagation criterion has been based on critical principal stress values, as well as fracture strain criterion. If the equivalent plastic strain exceeds a fracture strain based on appropriate chip material conditions, a crack will form. The selection of a path through the elements is an issue, for the geometric limitations of the elements restrict crack propagation path to the element surfaces. Algorithms used select a path as close to the real path as possible by satisfying criterion specific to each model. A good example of crack propagation when equivalent plastic strain ε_p exceeds the fracture strain ε_F is presented in figure 3.3.3.

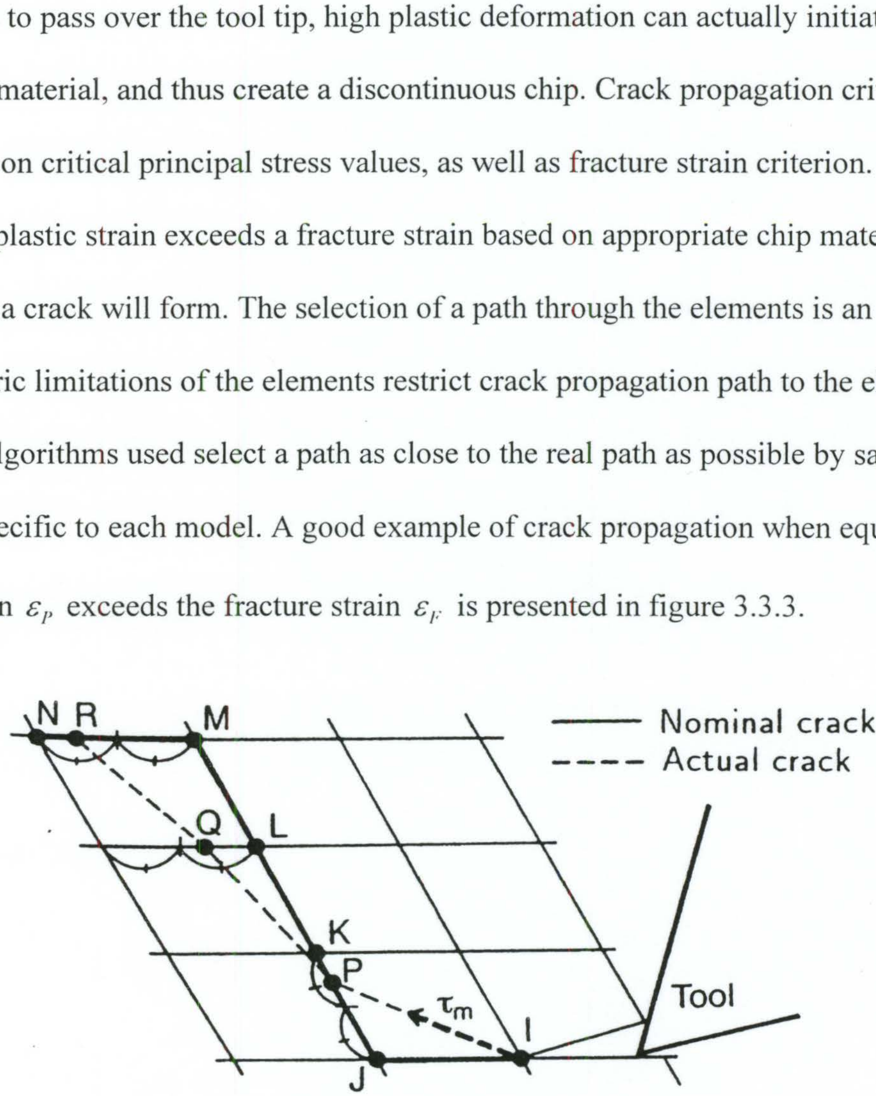

Figure 3.3.3 Introduction of a crack into the finite element (Obikawa and Sasahara, 1997).

Pathway selection is defined when the actual crack passes though an element boundary, on either side of the boundary midpoint. The nominal crack then is defined along the borders that most accurately represent the actual crack vector. Criteria are model specific, and so this explanation is simplified to convey only basic principals. When these new surfaces are created, frictional interaction between them is an important consideration. Very few models are able to create the slide lines on the new surfaces needed to simulate frictional forces. At higher speeds, this mechanism can have a large effect on the shape of the chip and the cutting forces involved in the process. The propagation of a fracture follows the crack initiation criterion closely. A fracture will often form near the tool tip and grow in the direction of the dynamic *(rotating)* shear plane until the chip surface is reached and complete chip separation occurs (figure 3.3.4).

3.3.6 Residual Stresses and Strains in the Machined Layer

It is known that residual stresses and strains in the finished workpiece are highly dependent on nodal separation criterion. The closer the separation takes place to the tool tip, the more plastic deformation and tool forces are transferred to the finished surface. In a discontinuous process, there are large builds and drops of plastic strain rate near the tool tip as chips separate from the workpiece and new chips begin to be formed. The contact area involved at the tool tip will concentrate forces when it is small and distribute them when large. Hence, as the chip is separated, there is a small contact area at the tool tip as the tool digs into the workpiece figure 3.3.5(a). The plastic strain rate will be high in this small region until the chip is formed 3.3.5(e). As crack propagation occurs, the strain rate and tool forces will drop drastically until workpiece penetration occurs again figure 3.3.5(f). This process leaves peaks and drops in the residual stress and plastic strain left in the finished surface (figure 3.3.6).

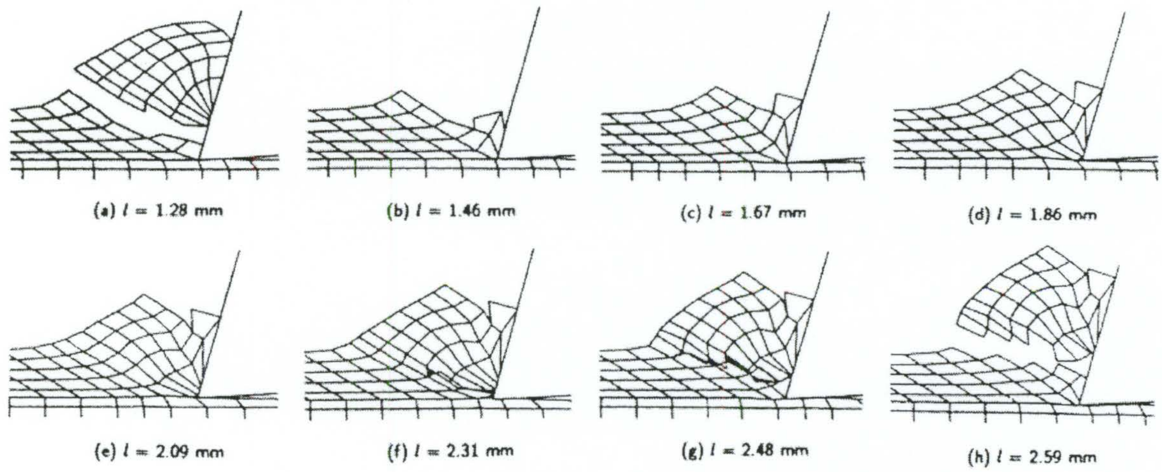

Figure 3.3.4 Finite element deformation and crack propagation in the modeling of discontinuous chip formation (Obikawa and Sasahara, 1997).

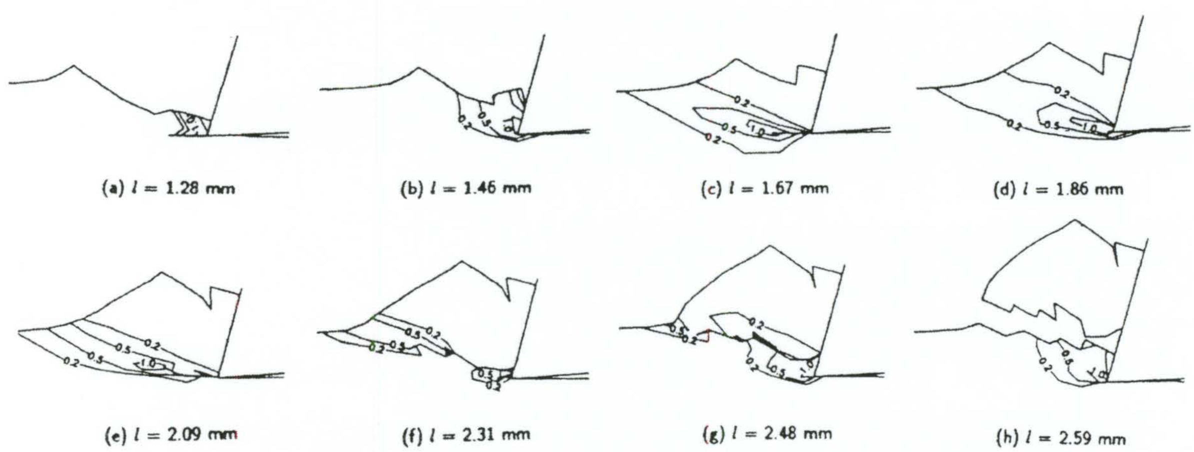

Figure 3.3.5 Distribution of the equivalent plastic strain rate in s^{-1} calculated during the second chip segmentation of brass (Obikawa and Sasahara, 1997).

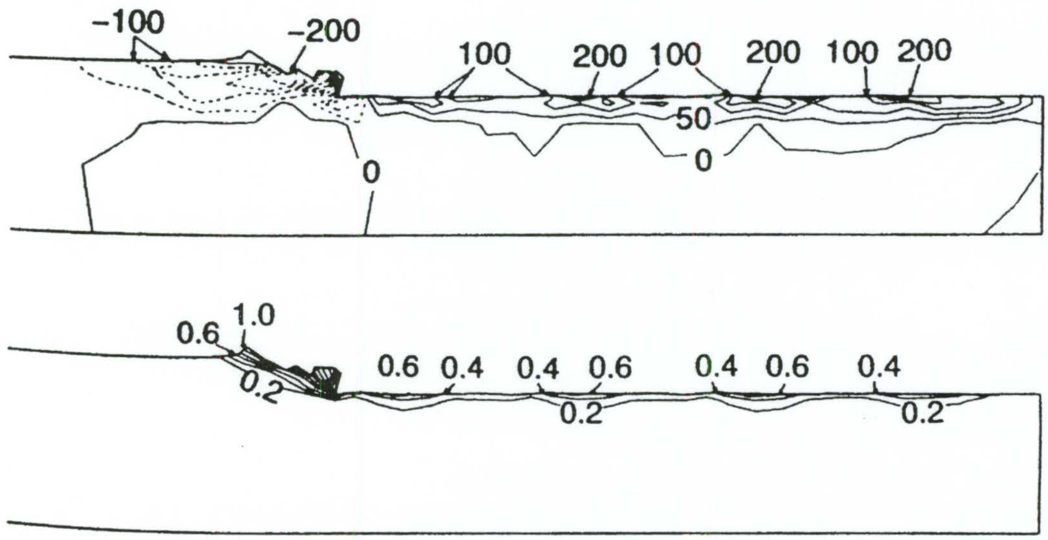

Figure 3.3.6 Residual stress σ_x in Mpa, and equivalent plastic strain in the discontinuous chip formation of brass (Obikawa and Sasahara, 1997).

CHAPTER 4

MATERIAL MODELING

4.1 Modeling of Material Behavior in Machining Processes

The high speed machining of AISI 4340-alloy steel involves complex non-linear deformation. High temperatures, stresses, strains, and strain rates dramatically affect the material properties and accordingly the deformation field. In order to model high speed machining, the material properties of the workpiece must be known under a wide range of extreme conditions. Thus, a constitutive model that takes into consideration the effects of temperature and strain rate must be numerically implemented in order to relate strain and stress. Fracture processes under high speed machining conditions must also be represented accurately and modeled using existing finite element methods. This must be applied to fracture both ahead of the tool tip and in the shear band. Adiabatic shear must also be captured in order to model segmented chip formation. This localization of shear instability can be numerically treated if again a valid constitutive model is used.

4.1.1 Constitutive Data for AISI 4340

The plastic deformation properties of an AISI 4340-alloy steel tempered at 550°C subjected to high temperature and strain rate loading conditions were studied in detail by

Lee and Yeh (1997). The deformation behavior at strain rates from 500 to 3300 s^{-1} and under constant temperatures in the range of 25 to 1100°C was studied using split Hopkinson bar testing (figure 4.1.1). While the strain rate of the loading fell far below the values experienced in machining, the use of this data was justified as data with similar coefficients were found in literature with applications to the simulation of high-speed metal cutting (Lovell, Bhattacharya, and Zeng, 1998). While the strain rates tested were not as high as those experienced in machining, the constants obtained were in good agreement with higher strain rate tests found in literature. Both scanning and tunneling electron microscopes (S.E.M and T.E.M) were used to examine the micro structural and fracture characteristics of the deformed specimens. Using analysis techniques and the data obtained from experiment, the authors fit the appropriate constants for a Johnson and Cook constitutive equation. This equation incorporates the effects of temperature, strain rate, and work hardening rate in its description of the plastic deformation behavior of the material.

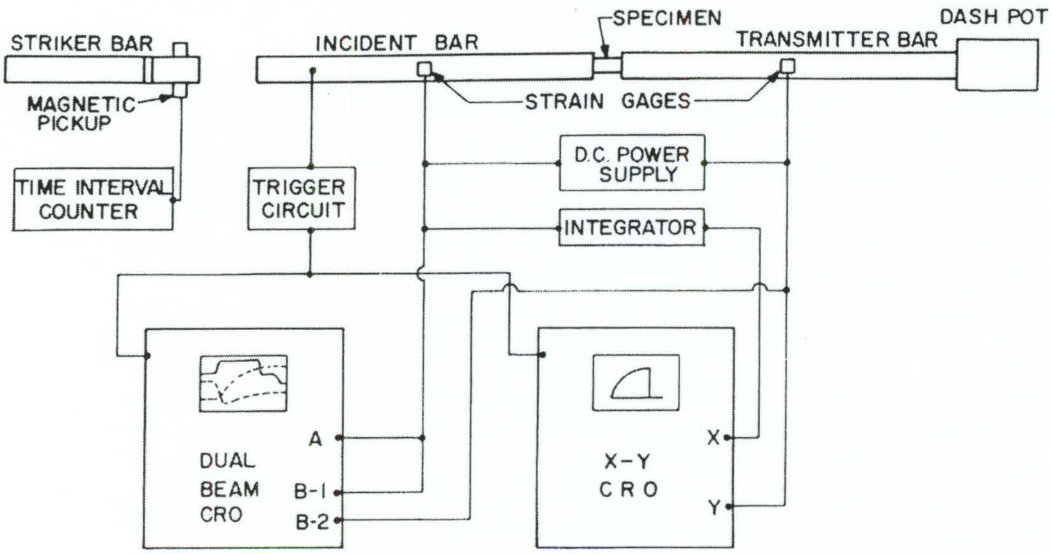

Figure 4.1.1 A schematic diagram of apparatus and instrumentation for a compression split Hopkinson bar test (Lee and Yeh, 1997).

The flow stress of AISI 4340-alloy steel was found to increase with the strain rate and decrease with the augmentation of temperature. The work hardening coefficient, strain rate and temperature sensitivities were also found to vary with the variation of strain rate, strain and temperature. The Johnson Cook constitutive equation resolves the flow stress σ for a specific state and time increment (Lee and Yeh, 1997). It is presented in the following form

$$\sigma = \left[A + B\varepsilon^{n}\right]\left[1 + C\ln\left(\frac{\dot{\varepsilon}}{\dot{\varepsilon}_O}\right)\right]\left\{1 - \left[\frac{(T - T_O)}{(T_m - T_O)}\right]^{m}\right\} \qquad (4.1.1)$$

where the where A, B, n, C, and m are the constants determined using a regression analysis of experimental data. T, T_O, and T_m are the current, the initial reference, and the melting temperatures respectively. The constant A represents the initial yield stress of

4.1.2 Fracture data for AISI 4340

All of the compression test specimens were broken in an adiabatic shear failure mode for conditions below 700°C and above a strain rate of 2700 s^{-1}. This type of failure is typical in nature to that experienced in the high speed machining of AISI 4340 alloy steel. A relation between compressive hydrostatic pressure and the fracture strain ε_F at low strain rates was experimentally established as

$$\varepsilon_F = -(1.0e-9)p + 0.77 \qquad (4.1.2)$$

using standardized tensile testing procedures (Zok and Embury, 1988). It was found that this criterion preformed poorly in its implementation into the modeling of machining. This was the first of many attempts at modeling fracture. Many criteria such as effective plastic strain, Von-Mises stress, and maximum principal stress were used to find misleading results. Each of these was then coupled into a function that limited the critical fracture value as a function of hydrostatic pressure. This improved results dramatically but not to the level needed. Fracture was then modeled within this work using both brittle and ductile fracture criteria. Brittle fracture was based on the fracture toughness model, where σ_f is the critical fracture stress, K_{IC} is the toughness, and l is the spacing between grain boundary carbides, typically on the order of two grain diameters (equation 4.1.3). Ductile fracture was based on a simplified Rice and Tracey criterion (equation 4.1.4) where ε_f^p is the critical effective plastic strain, ρ is the pressure, and $\bar{\sigma}$ is the effective Von Mises stress (Marusich and Ortiz, 1995).

$$\sigma_f = \frac{K_{IC}}{\sqrt{2\pi l}} \qquad (4.1.3)$$

$$\varepsilon_f^p \approx 2.48e^{-1.5\rho/\bar{\sigma}} \tag{4.1.4}$$

4.1.3 Adiabatic Heating and Shear Localization

During plastic deformation, the majority of plastic work is converted into heat. If the strain rate is high or the material has low thermal conductivity, there is insufficient time for the heat generated to dissipate into the surrounding material. Under these conditions, the localization of heat will cause thermal softening which will then in turn increase material flow that will result in even more heat generation. If this thermal softening effect is greater than the strain hardening effect, a localized thermal instability will occur and a thin band with very large adiabatic shear deformation will be observed.

Adiabatic shear bands are where failure is most likely to occur. Fracture occurs, from a micro structural point of view, due either to ductile void nucleation, growth, and coalescence, or by brittle cracking. Initiation sites of shear localization are known to be related to the homogeneity of the material due to the inclusion of defects or second phase particles such as carbides. Other causes of initiation are related to the release of dislocation pileups, geometric softening due to the rotation of atomic planes towards orientations with a lower Schmid factor, and preferential slip paths produced by martensite transformation and twinning (Lee and Yeh, 1997).

4.1.4 Material Modeling and Numerical Implementation

A strain rate and temperature sensitive Elasto-Plastic Johnson Cook constitutive material model was programmed and included in the FEA code H3DMAP by its originator, Richard Sauvé in December of 1999. This algorithm was tested and modified by the author and Farid Abrari in order to model transient high speed machining processes while using realistic computational resources. The constants supplied by Lee and Yeh (1997) for AISI 4340 were implemented and tested. This material model is basically a power law model that incorporates strain rate sensitivity with a temperature dependence assuming adiabatic heating due to the dissipation of plastic work (Sauvé, 1999). The material temperature is calculated based on element internal energy where the plastic work is converted into heat. A constant material specific heat C_p and density ρ is assumed and the material temperature T in an element is calculated as

$$T = T_{amb} + {E_V}/{C_p \rho} \qquad (4.1.5)$$

where E_V is the internal energy per unit volume. A density of 7830 kg/m^2, a material specific heat of 600 W/m*K, and an ambient temperature of 293.0 degrees Kelvin were used within this work to model the machining of AISI 4340 alloy steel.

CHAPTER 5

COMPUTATIONAL MODELING OF THE MACHINING OF AN AISI 4340 STEEL

The machining of a high strength AISI 4340-alloy steel tempered at 550°C was modeled using the finite element methods outlined within this work. The effects of specific cutting conditions on the resulting forces, stresses, strains, temperatures, workpiece surface, residual stresses, and chip morphology were studied. The formation of segmented chips at high cutting speeds and under aggressive cutting conditions was also modeled within this computational machining study. The results of this study were compared with simulations produced by 3rd Wave Systems (1999) 1and were obtained via a demonstration copy of their machining modeling software. This commercial software is based on the work by Marusich and Ortiz (1995) and has been benchmarked and calibrated for various materials including AISI 4340 for 2-dimensional analysis.

5.1 Assumptions

The machining process modeled was an orthogonal cutting operation. Current accepted models for machining define this as a plane strain operation provided the experimental procedure and analysis are preformed as outlined by Komanduri and Brown (Komanduri and Brown, 1981). This operation was assumed to have a plane strain condition throughout the workpiece and the tool material. This was achieved by fixing the degree of freedom in the Z-direction, hence restricting any strain deformation through the thickness of the model. This assumption is widely accepted and was used in order to compare the study with existing orthogonal analytical and numerical metal cutting models.

The tool was assumed perfectly rigid with a degree of freedom for velocity assignment in the X-direction. This assumption neglected tool dynamics and the elastic deformation of the tool. While tool dynamics and deformation have an effect on the finished workpiece surface in machining operations, the need to decouple these effects was apparent, as currently existing orthogonal analytical and numerical metal cutting models do not address these issues. Dynamics and tool deformation are to be analyzed in future work and their effects will be assessed based on cutting conditions.

Workpiece surface curvature was neglected in the simulations. This assumption was made due to the scale of the problem, where the curvature on the surface was found to be negligible in comparison with the scale of the simulations. The problem was also discretized into a finite volume with appropriate boundary conditions applied to the far field surfaces. The workpiece was fixed in all degrees of freedom on the lower X-Z plane surface and the rightmost X-Y plane. All of the nodes in the workpiece were also fixed in the Z degree of freedom. This induced a plane strain condition. These assumptions are widely accepted in the field of the modeling of machining processes using both finite elements and standard analytical models.

5.2 Initial Conditions

A three-dimensional workpieces and tools were constructed and discretized into finite element meshes as shown in figure 5.2 and figure 5.23. The finite element meshes were constructed using eight noded hexahedral elements. These three dimensional cube shaped elements use an under-integrated single interpolation point located at the center of the element volume to linearly interpolate the displacement field. Master contact surfaces were defined on all of the outward normal faces of the tool. The workpiece volume was defined in terms of contact pair relations as a cloud of slave nodes coupled to the master contact surfaces of the tool. This allowed for new surface generation to include contact with the tool while allowing fracture to propagate through the finite element mesh. Element size in the workpiece was varied based on the type of analysis to be preformed. The lower surface of the workpiece on the X-Z plane was constrained in all directions. The left most X-Y surface of the workpiece was also constrained in this manner. The upper and rightmost surfaces of the workpiece were left unconstrained except for the imposed plane strain condition throughout the volume. Each tool was positioned according to cutting conditions and was assigned a specific cutting velocity.

The mass of the material was artificially scaled in order to increase the speed of the transient solution. This technique is commonly applied in explicit methods. By artificially scaling the mass, the speed of sound in the material is increased such that a larger time step can be used while still maintaining solution stability. This scaling has it limits though, as it was found that the results became unstable and inaccurate if the tool velocity approached 1% of the elastic wave speed (*speed of sound*) in the material. In such a case, the elastic waves have little time to propagate from the loading front and constructive wave interference occurs. This causes the elastic wave energy to build leading to the destabilization of the solution.

5.3 Cutting Conditions

Finite element models with the cutting conditions outlined in table 5.1 were constructed in order to simulate both continuous and discontinuous chip formation experienced in the machining of AISI 4340. This route was chosen in order to prove the applicability of finite element machining simulations to both process optimization on a production floor, and to the prediction of the effects of cutting conditions on a manufactured component. Such a study in a larger form offers dramatic savings in terms of tooling, materials, and downtime for a floor tooling up for a new process or procedure. These results would also help close the loop between the design and manufacturing stages of machined components, as residual stresses are known to have an effect on the fatigue life and performance of a component.

Test Number	Rake Angle (deg)	Flank Angle (deg)	Depth of Cut (mm)	Feed (mm)	Tip Radius (mm)	Cutting Speed (m/s)
1	+ 10	+ 7	0.25	1	0.025	6.667
2	0	0	0.254	0.1	Sharp	6.667
3	0	0	0.5	0.1	Sharp	8.333

Table 5.1 Cutting conditions for each simulation.

5.4 Friction Conditions

5.4.1 Coulomb's Law of Friction

The application of friction between the tool and workpiece was modeled using Coulomb's law of friction. Coefficients of friction for both static and dynamic friction were applied to the contact surfaces. The generalized coefficient of friction using the supplied constants was determined during simulation using the equation

$$\mu = \mu_d + (\mu_s - \mu_d)^{(-\dot{x}_{rel} c_v)} \qquad (5.1.1)$$

where μ is the coefficient of friction, μ_d is the dynamic coefficient of friction, μ_s is the static coefficient of friction, c_v is the exponential smoothing coefficient, and $\dot{x}_{rel}$ is the relative velocity of the sliding surfaces. This velocity dependant model for the coefficient of friction permitted both static and dynamic coefficients of friction to be included (Sauvé, 1999).

It was found that the friction forces generated on the rake face often exceeded the maximum shear flow stress of the workpiece material, which in turn generated excessive shear deformation in the elements in contact with the rake face. Due to the explicit nature of the solution and the conditional stability limit inherent to this method, this was unacceptable. The elements on the rake face were the always the ones imposing the minimum time step on the solution. While the secondary shear zone is known to be a zone of extremely localized shear, the element resolution needed to resolve a friction interface at a micron scale was not possible due to computational expense. Nor was the need to resolve this interface legitimate as the friction model captured the work and hence the heat due to friction on this extremely narrow contact interface. The secondary shear zone deformation field still captured the strain in this region accurately when a limit on the maximum amount of frictional shear stress was applied. When the amount of shear stress generated on the friction contact surface exceeded the maximum shear stress of the workpiece material, sliding was induced such that tangential friction force generated a the shear stress on the surface slightly lower than the specified limit. This is a classical procedure for the application of stick slip friction simulation in the finite element simulation of metal cutting and examples in literature are widespread (Marusich and Ortiz, 1995). The friction and contact parameter conditions applied for each of the cutting tests are outlined in table 2.

5.4.2 Contact Damping:

When using a penalty method to model contact and friction interface conditions, the integration into an explicit method offers challenges in terms of solution stability. It was found that the undamped motion of slave nodes penetrating a master contact surface caused high frequency instabilities when large penalty forces were imposed. Large penalty forces being applied by the contact algorithm were a symptom of the high loading gradients and highly non-linear conditions experienced in metal cutting. The solution stability of the explicit method was affected dramatically if a slave node was accelerated quickly as the element it was attached to would go super-plastic within a few time steps. This super-plastic state had the tendency to put elements into an unstable hourglass mode in which solution stability was seriously compromised to such a point that the simulation was halted.

The application of a velocity based damping algorithm to the applied motion of a slave node being accelerated out of a master surface had a dramatic effect on solution stability. Different damping coefficients were applied and were selected based on the control conditions of the model, such as cutting velocity and the artificially scaled mass.

Test Number	Penalty Stiffness Factor	Static Coefficient of Friction	Dynamic Coefficient of Friction	Exponential Coefficient of Transition	Velocity Damping Coefficient
1	0.3	0	0.5	0.1	0.5
2	0.1	0.4	0.5	0.1	0.0
3	0.1	0.5	0.4	0.1	0.0

Table 5.2 Friction and contact parameters for each simulation.

5.5 Initial Geometries and Meshes

The initial configurations of the tools and the workpieces are illustrated in figures 5.1. and 5.23. The tool was positioned at the appropriate depth of cut such that the undeformed chip thickness was equal to that specified in table 5.1. Table 5.3 shows the initial dimensions of and the number of elements contained within each of the test workpieces. The tools were meshed with a bias towards the tool tip such that more elements were concentrated near this point. While this was a useful exercise to be used in future work, it had no immediate purpose in these simulations as the tool was modeled as an ideal rigid body. The tool used in test number 1 was given a tool tip with a slight radius in order to model either a slight amount of wear or an edge preparation (table 5.1).

Test Number	Workpiece Dimensions (mm)			Number of Elements in the			Min. Element Size (mm)
	X-Dir	Y-Dir	Z-Dir	X-Dir	Y-Dir	Z-Dir	
1	+ 6	- 1	+ 1	75	25	1	0.08
2	+ 3	+ 1	+ 0.1	250	75	1	0.012
3	+ 3	+ 1	+ 0.1	250	75	1	0.012

Table 5.3 Dimensions and element information for each of the workpieces.

5.6 Failure Models

The specifications for the failure models used in each of the tests are outlined in table 5.4. The workpiece used in test number 1 was given a layer of erodeable elements two layers thick in the path of the lowermost point of the tool tip. This was done, as element erosion tends to cause excessive volume loss during the transition into steady state chip formation. In order to produce a realistic continuous chip, this layer had a need to be localized in front of the tool tip. In the case of the other two tests, all of the elements in the workpiece were designated erodeable in order to model segmented chip formation.

5.7 Results of Continuous Chip Formation Simulation 1

The simulation was run for a cutting duration of 6.0E-4 seconds and took approximately 2.5 hours to solve on a single Silicon Graphics 400 Megahertz processor.

This processor was contained within an Origin machine and less than 40 Megabytes ram was used for the solution. Solution stability was low such that only a few of many simulations were successful. The current contact algorithm and the lack of continuous remeshing are currently the major causes of solution instability for machining applications.

Test Number	**Failure Model:** $\varepsilon_f^p \approx (A)e^{-(B)p/\bar{\sigma}}$	**1st Coeff. (*A*)**	**2nd Coeff. (*B*)**	**Von-Mises Minimum for Failure**	**Erodeable Elements**	**Number of Timesteps Until Failure**
1	Rice & Tracey	1.5	-1.5	250 MPa	2 Layers	10
2	Rice & Tracey	2.48	-1.5	500 MPa	All	10
3	Rice & Tracey	2.48	-1.5	500 MPa	All	10

Table 5.4 Failure model specifications for each of the simulations.

5.7.1 Deformed Mesh and Chip Morphology

A 2-dimensional view of the deformed mesh as shown in figure 5.3 was run for a cutting duration of 6.0E-4 seconds. A 3-dimensional view is illustrated in figure 5.7 at a cutting time of 3.0E-4 seconds. The simulation was successful in producing a continuous chip with both a realistic shape and curl. The deformed chip was thicker than that of the un-deformed chip thickness as expected and a cutting ratio of 0.625 was calculated using these measurements. Using the cutting ratio and equation 2.14, the shear angle was calculated to equal 35 degrees. The deformed mesh and chip morphology was compared with the results of a commercial finite element package called 3rd Wave Systems used to simulate orthogonal metal cutting (figure 5.4). The cutting conditions between the two simulations were only slightly different, with the differences listed in table 5.5. The differences in the chip shape and curl were minor, and these were directly related to the different rake angle and the tool breaker respectively. Animations and different stages of this chip formation process for both simulations were viewed and results were generally in excellent agreement.

Differences in Cutting Conditions for Simulation 1						
Simulation	**Cutting Speed V(m/s)**	**Rake Angle (deg)**	**Flank Angle (deg)**	**Feed (mm)**	**Edge Prep. Radius (mm)**	**Tool Shape**
H3dmap	6.667	+ 10	+ 7	2.5	0.25	Conventional
3rd Wave	6.667	0	+ 5	2.54	0.25	With Breaker

Table 5.5 A comparison of the cutting conditions used in the author's work and in the results of a commercial package.

5.7.2 Effective Plastic Strain

A 2-dimensional plot of effective plastic strain at a cutting time of 6.0E-4 seconds (figure 5.5) was in good agreement with the same plot generated by 3rd Wave Systems software (figure 5.6). A maximum effective plastic strain of 4.68 neglecting singularities generated at initial contact was obtained using the heavily modified version of H3dmap, which was in good agreement with the benchmarked software's value of 4.0. The effective plastic strain was greatest as expected in the elements just exiting the secondary shear zone located on the rake face of the tool. Since strain is a accumulative history based value, the value will be the greatest after an element passes through first the primary shear band and afterwards the secondary shear band. A 3-dimensional contour plot of effective plastic strain at a cutting time of 3.0E-4 seconds is illustrated in figure 5.8. Both the H3dmap plots clearly show the location of the primary shear band at an angle of 35 degrees, which was in exact agreement with the value calculated using the cutting ratio and the rake angle (equation 2.14).

5.7.3 Temperature

A 2-dimensional plot of temperature is shown in figure 5.9 and is compared with the benchmarked software in figure 5.10. It is interesting to note effective plastic strain is also analogous to adiabatic heat, as the heat generated due to work other than interface friction will be captured totally in the plastic work of an element. By using equation 4.1.5 and replacing the internal energy per unit volume E_V with the yield stress multiplied by the effective plastic strain (obtaining the plastic work energy), the adiabatic heat in the model was calculated. Current work by the author and affiliated research group is focused on thermally coupling H3dmap with a thermal analysis software H3dtap in order to take heat conduction, heat due to friction, and the effects of coolant into consideration.

Large differences in the maximum values found for temperature exist between the two different modeling packages. This is due to the fact that H3dmap does not currently take the heat generated by the work due to friction into consideration. Hence the temperatures found on the rake face will be significantly different. The majority of the chip is in agreement though, as the temperature in the primary shear band is around 300 degrees Celsius and the rest of the temperature contour shapes and temperatures are similar in distribution and magnitude through the deformed chip thickness. The mean values are slightly lower due to the difference in the cutting conditions between the two models, where it was expected and shown that the 0 degree rake angle in the 3rd Wave solution would generate a slightly higher cutting temperature. The difference in the chip curl aside from the cutter geometry effects can be attributed to the temperature due to the frictional work neglected in the H3dmap solution. As expected, a lower temperature on the rake face side of the chip generates a chip with less curl due to differences in volumetric thermal expansion.

5.7.4 Von-Mises Stress

A 2-dimensional plot of the Von-Mises stress calculated at 6.0 E-4 seconds is shown in figure 5.11 and compared with commercial software in figure 5.12. As expected, the maximum Von-Mises stress developed (962 MPa) is only slightly higher than the initial yield stress (950 MPa) of the material modeled. Once a ferrous material exceeds its initial yield stress, the stress developed beyond this value is due to strain or strain rate hardening processes. The Johnson Cook material model used captures these hardening effects and they are exhibited by the slightly higher than yield Von-Mises stress developed in the model. The comparison of the two modeling package results shows similarities in the distribution and magnitudes of this stress, but figure 5.12 shows a significantly higher maximum stress due to the stresses induced in the tool. From the results illustrated in figure 5.12, it seems that either the simpler material model based on power law hardening or a different initial yield stress generates a slightly higher Von-Mises stress in the shear plane. The H3dmap solution plot is quite "patchy" in appearance due to the extensive numerical noise or high frequency waves "ringing" in the material that had not plastically yielded. The 3rd Wave solution does not show this phenomenon due to the scale of the plot. Plastic material has a large tendency to damp this elastic wave ringing and hence the material that has exceeded yield in the shear plane is not patchy and is of the greatest interest. Figure 5.11 shows the shear plane clearly at approximately 35 degrees, which is in excellent agreement with prior calculations. In the future, damping or element refinement should be used to help reduce the noise in the solution but for the purposes of this initial work it was irrelevant.

5.7.5 Hydrostatic Pressure

A 2-dimensional plot of pressure was calculated and is illustrated in figure 5.13 and was compared with a 3rd Wave plot in figure 5.14. The hydrostatic pressures induced were in excellent agreement in magnitudes and distribution between the two models. Compressive pressure was found on the chip at the tool tip and on the back of the chip as expected. A compressive wave front was found in front of the tool and a tensile pressure was induced on the finished workpiece surface with a value of approximately 200 MPa. This is in good agreement with metal cutting theory and current values of experimentally measured residual stresses.

5.7.6 XX-Stress Component

The XX-stress component in the direction of cutting is usually used as a measure of the residual stresses left on a machined surface due to their dramatic effects on the fatigue life and quality of a component. Induced compressive stresses are desirable as they have a tendency to increase the stress a surface can sustain before plastic yield. Tensile stresses are more common to machined surfaces and hence any processes that can help reduce these values towards the compressive are desirable as they will be detrimental to the strength of the component. The tensile XX-stresses induced on the machined surfaces were in excellent agreement with the commercial package and were within expected values. Figure 5.15 shows the H3dmap solution and results in a tensile stress in the region of 250 MPa. This value would significantly lower the amount of tensile stress that the surface could sustain during operational service life.

5.7.7 YY-Stress Component

The YY-stress component calculated is illustrated in figure 5.17 and found to be in good agreement with the 3rd Wave solution shown in figure 5.18. A large tensile stress approaching the yield stress of the material was found on the back of the chip and at the tool tip as expected. A compressive stress was found on the rake side of the chip and can be attributed to the thermal expansion generated in this highly strained region. Hence the difference in the directions on these stresses across the deformed chip thickness cause the chip to curl into its final deformed state.

5.8 Results for Incipient Continuous Chip Formation Simulation 2

The simulation was run for a cutting duration of 7.5E-5 seconds and took approximately 4.5 hours to solve on a single Silicon Graphics 400 Megahertz processor. This processor was contained within an Origin machine and over 150 Megabytes ram was used for the solution. Solution stability was low such that only a few of many simulations were successful. The large transition to the beginnings of chip formation induced by a 0 degree rake angle had massive effects on the stability of the solution. The current contact algorithm and the lack of continuous remeshing are currently the major causes of solution instability for machining applications with this package.

5.8.1 Effective Plastic Strain and Chip Morphology

Figure 5.19 shows a comparison of the effective plastic strain as well as the chip morphology for a cutting test with the same cutting conditions as preformed by each of the different software packages. The chip shape and deformed chip thickness is the same for each of the simulations with a slight difference in the orientation due to the chip breaker geometry on the 3rd Wave tool. A cutting ratio of 0.5476 was calculated for both models and the shear plane angle was calculated as 29 degrees. This was in excellent agreement with the 29-degree profile of the shear band visible in both figures 5.19 and 5.20. The values of effective plastic strain were in excellent agreement with the exception of the value at the tool tip due which can be directly attributed to the loss of data inherent to the erosion of elements used to simulate separation and fracture in H3dmap.

5.8.2 Von-Mises Stress

Figure 5.20 shows a comparison of the Von-Mises stress induced in the models using both software packages. As in the previous simulation the maximum value of stress in the 3rd Wave solution was defined by the tool tip, as the tool was analyzed within this model. The stress distribution and magnitude is similar in both models but again as in the previous simulation, the stress in shear plane of the 3rd Wave solution is a little higher due to the simplier material model used or a difference in the initial yield stress of the material. A difference in the initial yield stress could also be due to a slightly different tempering of the AISI 4340 steel modeled.

5.9 Results for Discontinuous Chip Formation Simulation 3

The simulation was run for a cutting duration of 6.0E-5 seconds and took approximately 4.5 hours to solve on a single Silicon Graphics 400 Megaherz processor. This processor was contained within an Origin machine and over 150 Megabytes ram was used for the solution. Solution stability was quite high in this simulation as elements that approached deformation modes that would begin to restrict the solution were eroded due to adiabatic shear localization. The lack of a secondary shear zone formation under these cutting conditions producing this type of segmented chip (Komanduri and Schroeder, 1982) also helped to increase the solution stability. The current element erosion algorithm and it associated volumetric loss limit this approach and hence only the first segment produces accurate results. Segments formed after the first segment begin to loose too much volume due to the cumulative effect of plastic strain. When elements are deformed in the primary shear zone, they accumulate strain. When they continue to be deformed in the secondary shear zone, some elements on the rake face sustain sufficient strain to be eroded by the failure model. This effect becomes even more pronounced as the hydrostatic pressure in surrounding elements drops as an element is eroded. This lowers the hydrostatically dependent effective plastic strain failure threshold and elements that have previously exceeded this value erode. This results in a cascading volume loss in the secondary shear zone. Current work includes a revised surface generation and contact algorithm reassignment procedure that will treat this mechanical process without any associated volumetric loss and will dynamically create new contact surfaces.

5.9.1 Deformed Mesh and Chip Morphology

A 3-dimensional mesh showing the initial geometry and the final deformed geometry is shown in figure 5.21 at a cutting time of 0.0 and 6.0E-5 seconds respectively. The deformed mesh shows the adiabatic localization of shear in the shear plane until a failure surface is generated producing a segmented chip. The size and shape of the chip are in agreement with experimental (Komanduri and Schroeder, 1984) and numerical results found in literature with similar cutting conditions (Marusich and Ortiz, 1995). The shear-localized plane was found to initiate along a 45-degree angle and started to develop a slight curvature as chip formation progressed. As shown in figure 5.24 and 5.25 the comparisons of chip morphology are very close. Even the slight downward curvature at the top tip of the segmented chip is clearly visible in both models. Slight differences can be attributed to minor differences in the cutting conditions simulated as outlined in table 5.6.

Differences in Cutting Conditions for Simulation 3						
Simulation	**Cutting Speed V(m/s)**	**Rake Angle (deg)**	**Flank Angle (deg)**	**Feed (mm)**	**Edge Prep. Radius (mm)**	**Tool Shape**
H3dmap	8.333	0	0	5.0	Sharp	Conventional
3rd Wave	10.0	- 5	+ 10	5.0	0.25	Conventional

Table 5.6 A comparison of the cutting conditions used in the author's work and in the results of a commercial package.

5.9.2 Effective Plastic Strain and Adiabatic Shear Localization

Plots of the effective plastic strain induced in the author's simulation at different stages of chip formation are shown in figures 5.22 and 5.23. Plastic strain begins to localize in the shear band at the very beginning of chip formation. At this point temperature begins to dramatically rise in these deformed elements and they begin to thermally soften. This softening is counteracted by the strain and strain rate hardening effects captured by the material model, but thermal softening quickly dominates and the strain accelerates. The elements in this highly localized region approach a temperature of above 400 degrees Celsius before they begin to fail.

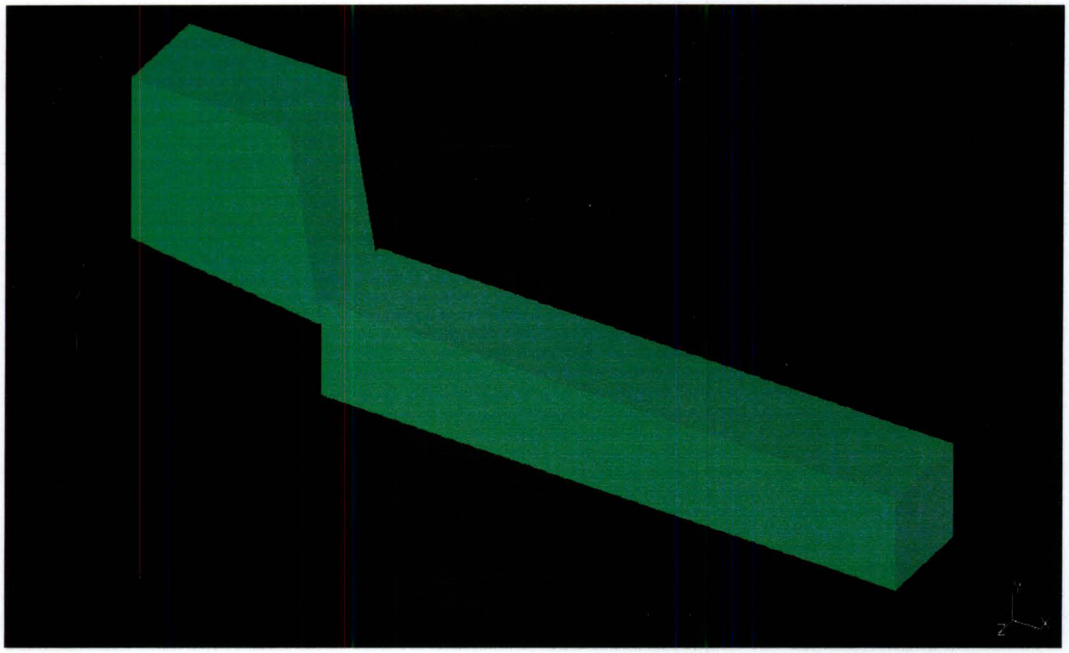

Figure 5.1 Initial tool and workpiece geometry and configuration.

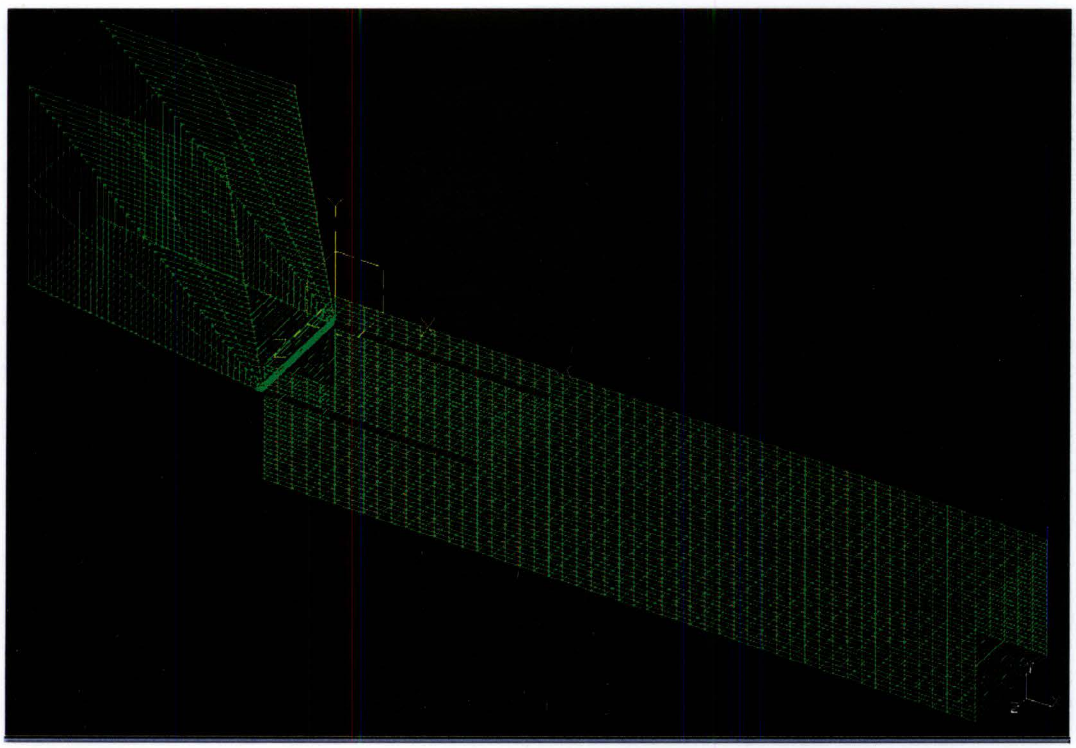

Figure 5.2 A 3-dimensional plot of the un-deformed workpiece and tool mesh showing elements that were eroded during and up to a time of 3.0E-4 seconds.

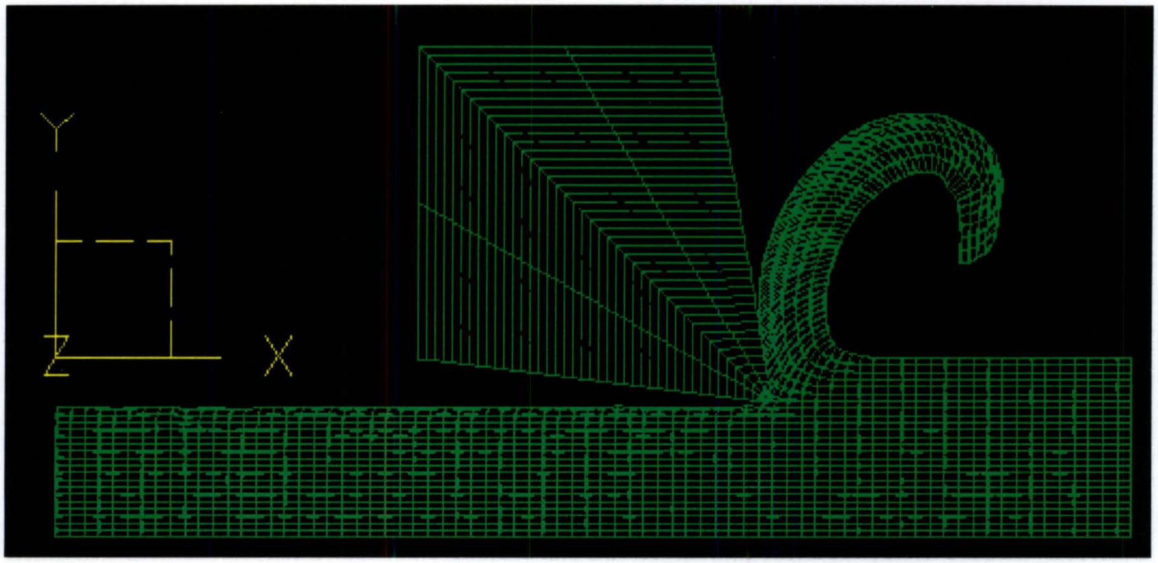

Figure 5.3 A 2-dimensional view of the final deformed mesh geometry at a time of 6.0E-03 seconds.

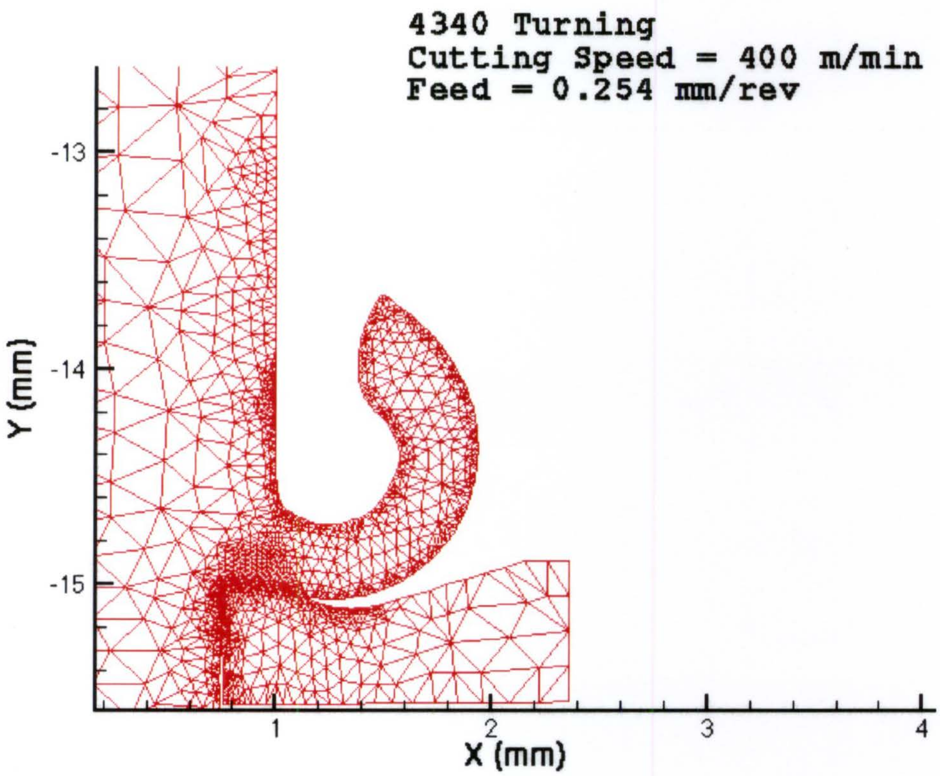

Figure 5.4 A deformed mesh as calculated by 3rd Wave Systems (1999).

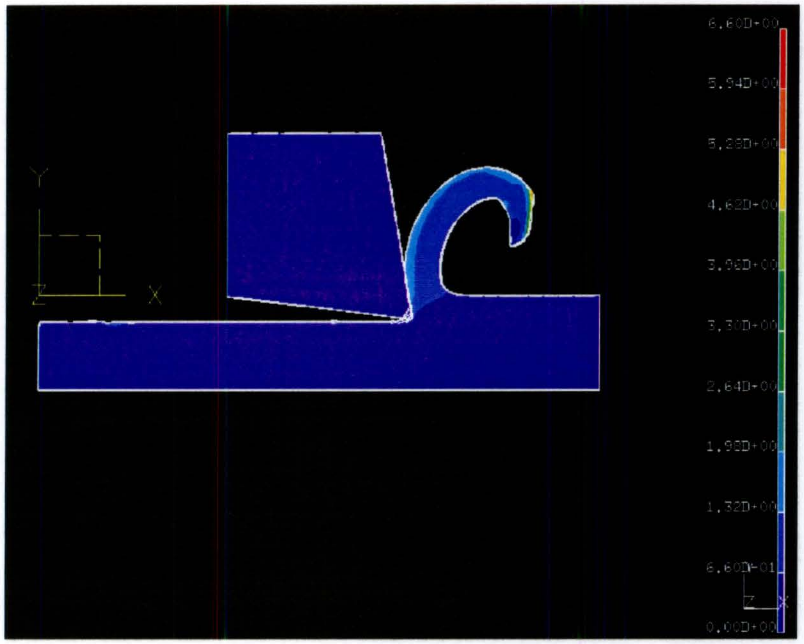

Figure 5.5 A 2-dimensional plot of effective plastic strain at a time of 6.0E-04 seconds.

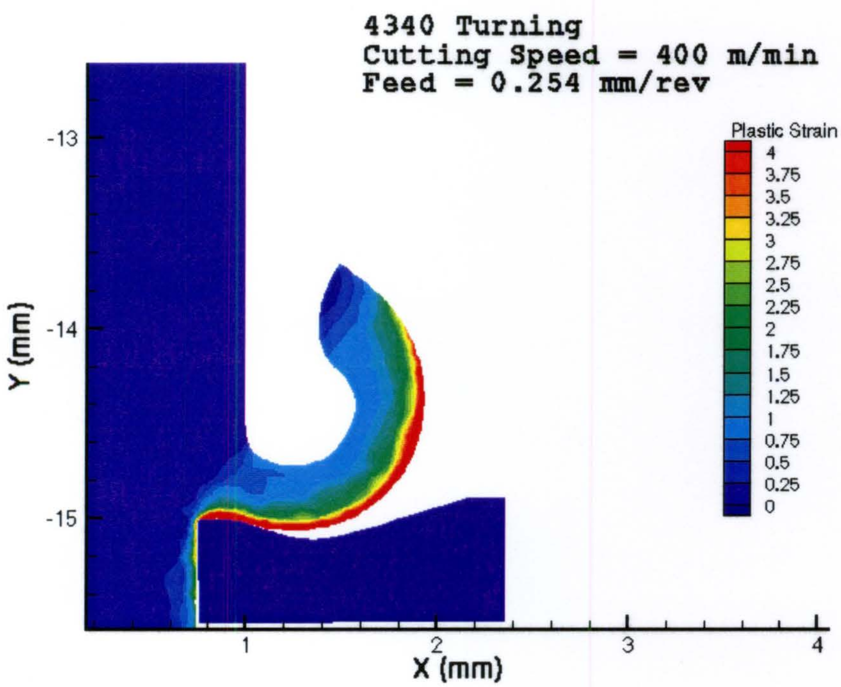

Figure 5.6 A plot of effective plastic strain calculated by 3rd Wave Systems (1999).

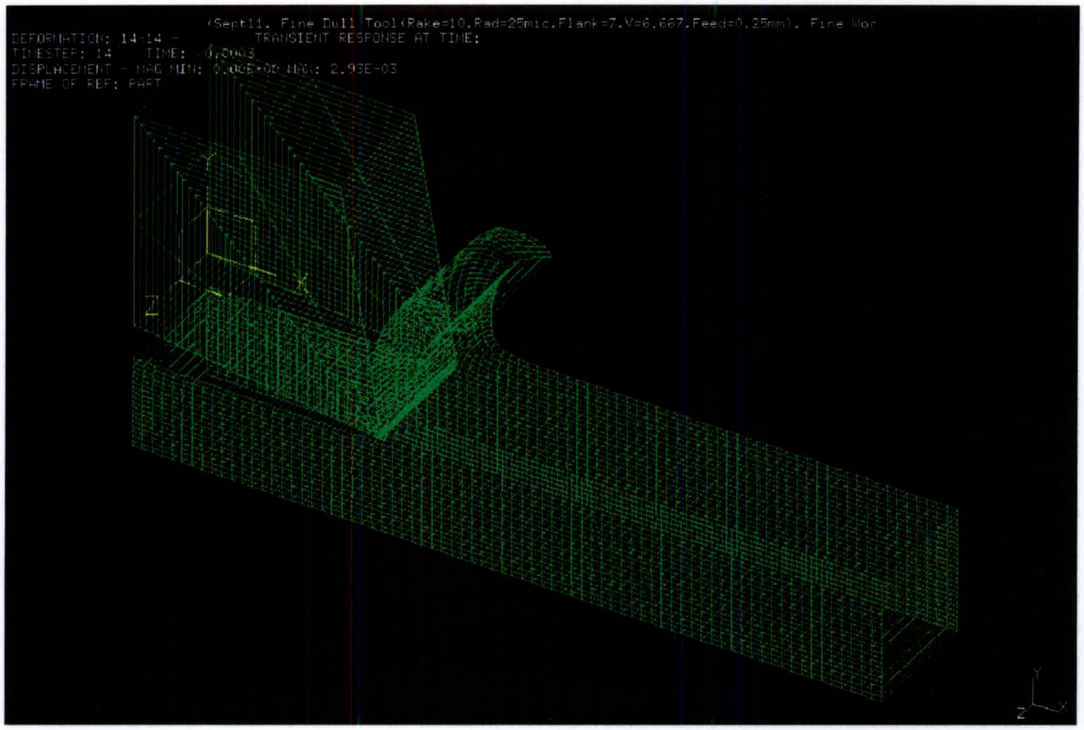

Figure 5.7 A 3-dimensional view of the deformed mesh at a time of 3.0E-04 seconds.

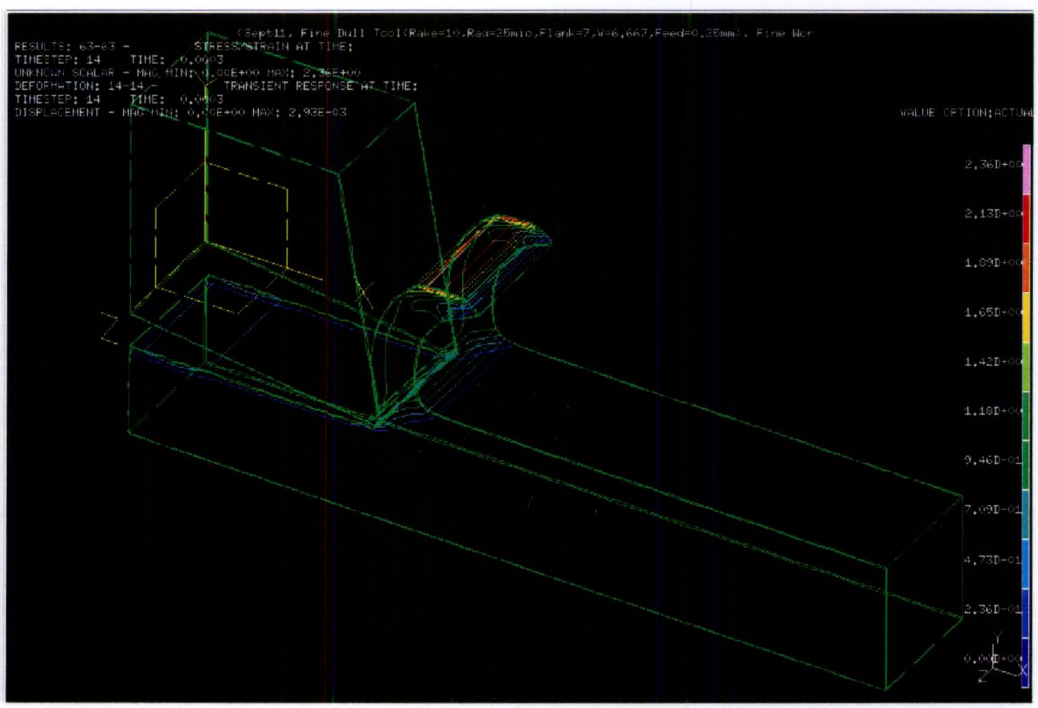

Figure 5.8 A 3-dimensional contour plot of effective plastic strain at 3.0E-04 seconds.

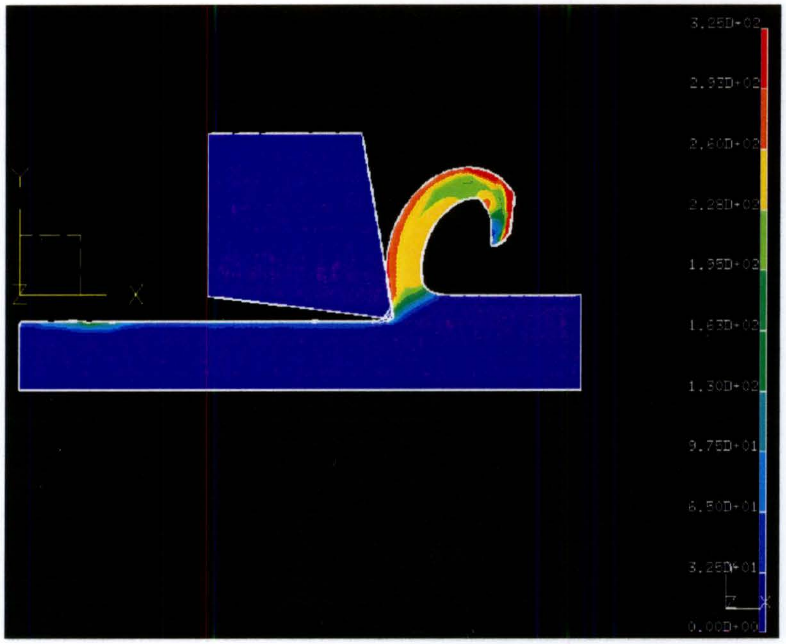

Figure 5.9 A 2-dimensional plot of adiabatic heat at 6.0E-4 seconds.

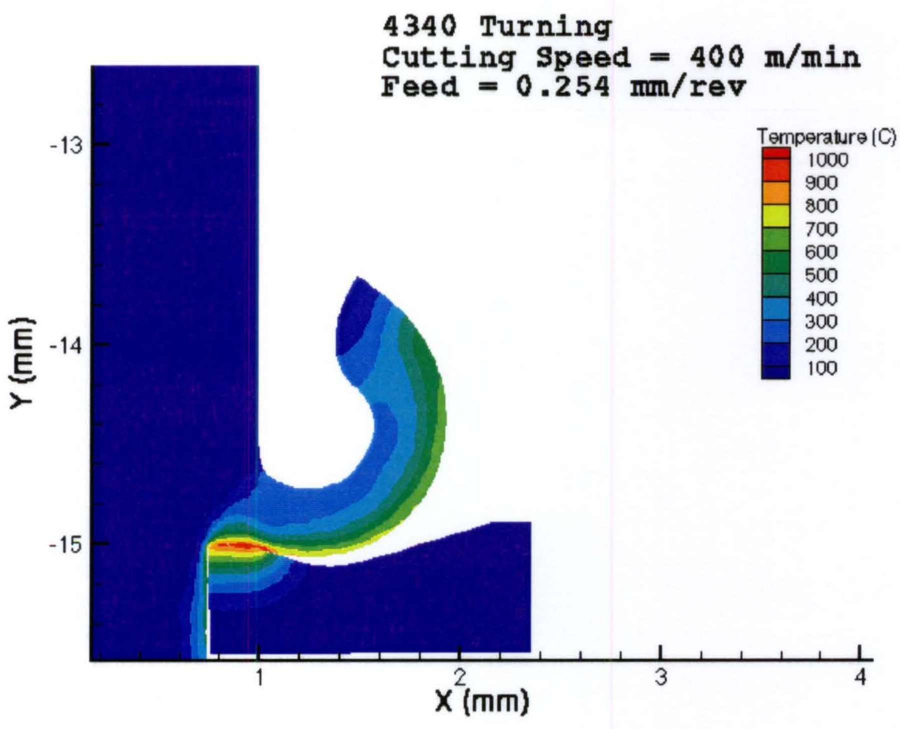

Figure 5.10 A plot of temperature as calculated by 3rd Wave Systems (1999).

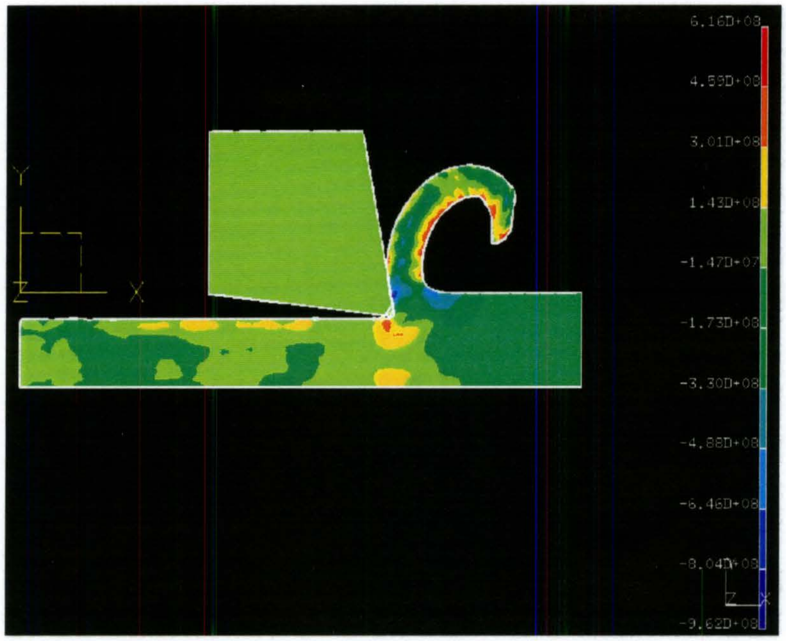

Figure 5.13 A 2-dimensional plot of hydrostatic pressure at 6.0E-4 seconds.

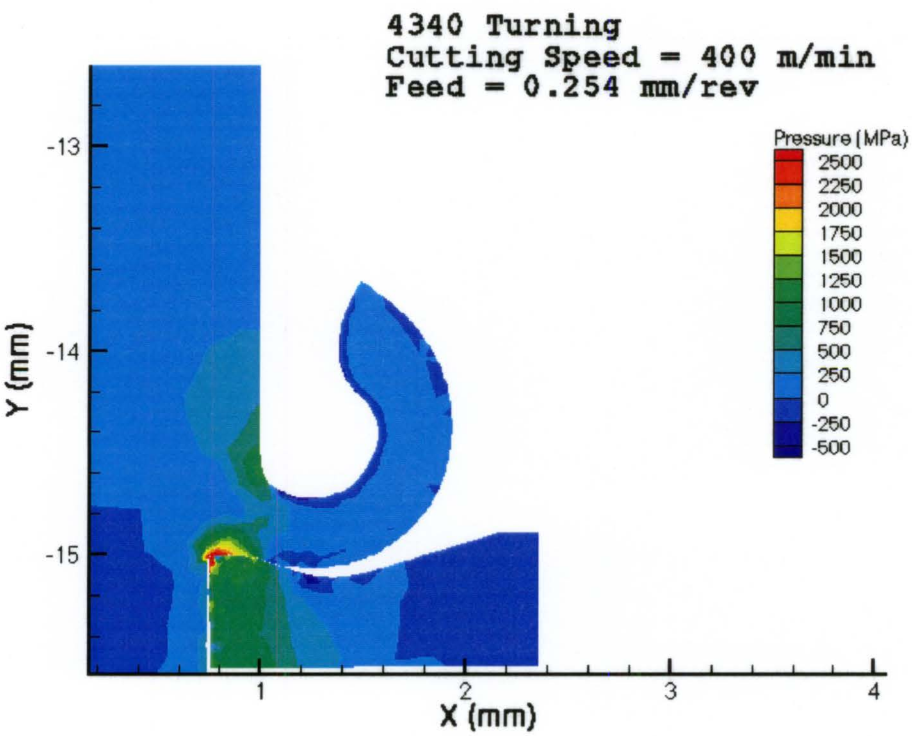

Figure 5.14 A plot of hydrostatic pressure as calculated by 3rd Wave Systems (1999).

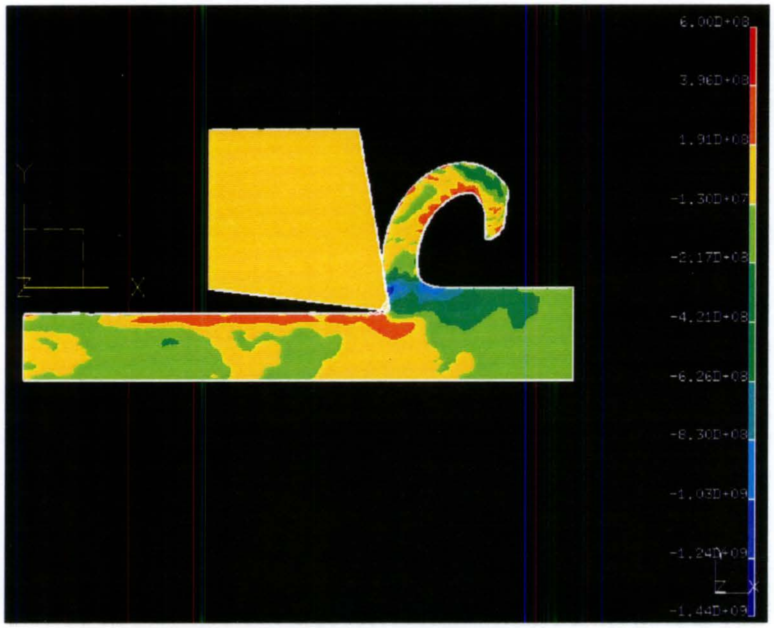

Figure 5.15 A 2-dimensional plot of the XX-stress component at 6.0E-4 seconds.

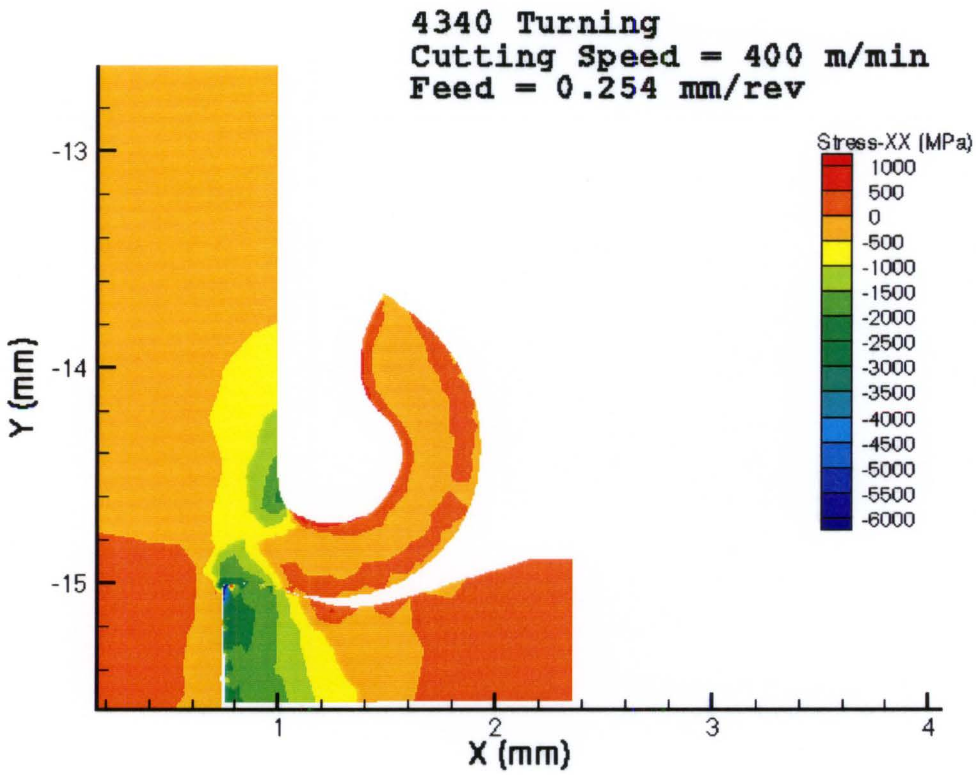

Figure 5.16 A plot of the XX-stress as calculated by 3rd Wave Systems (1999).

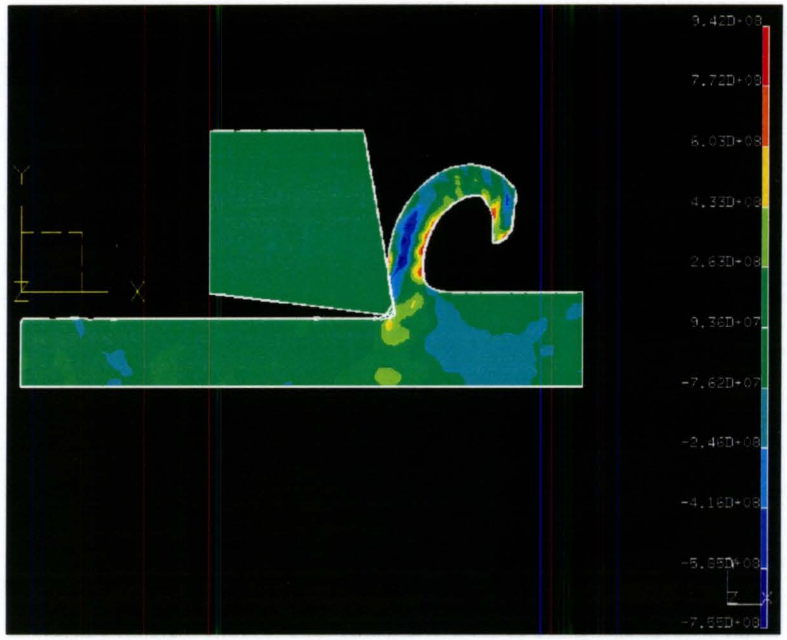

Figure 5.17 A 2-dimensional plot of the YY-stress component at 6.0E-4 seconds.

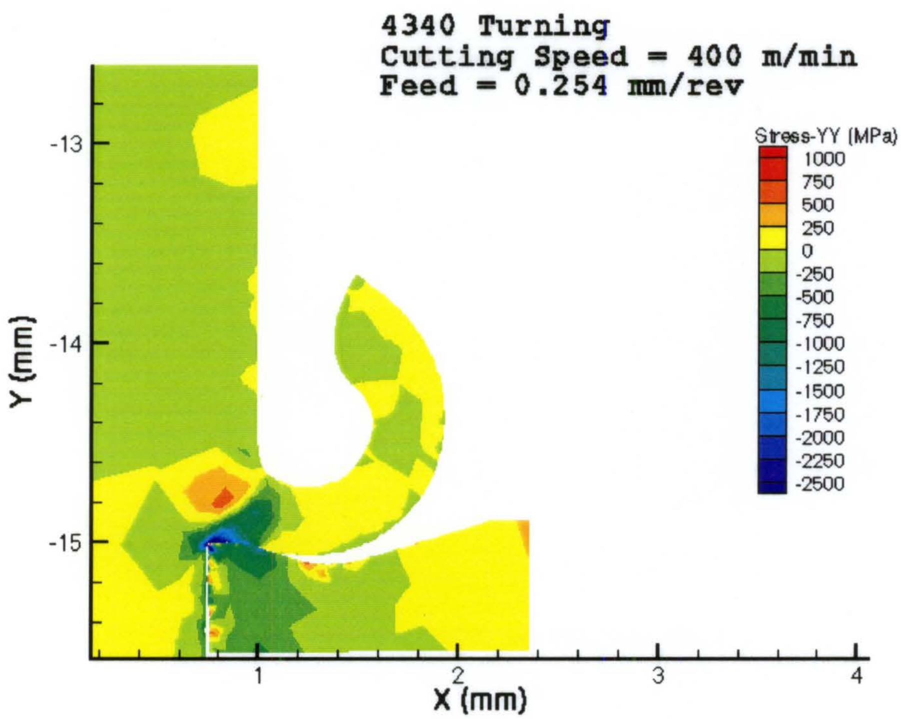

Figure 5.18 A plot of YY-stress as calculated by 3rd Wave Systems (1999).

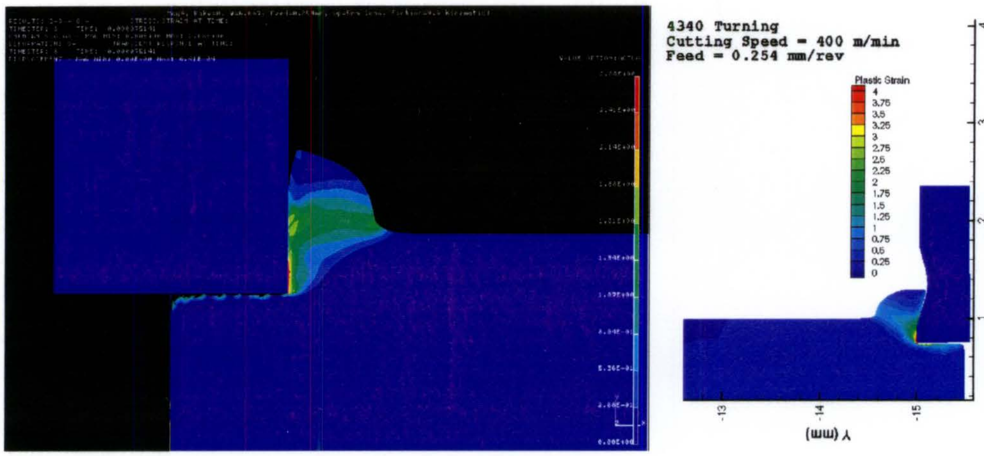

Figure 5.19 A comparison of plastic strain at early stages of chip formation as modeled by both H3dmap and 3rd Wave Systems under similar cutting conditions.

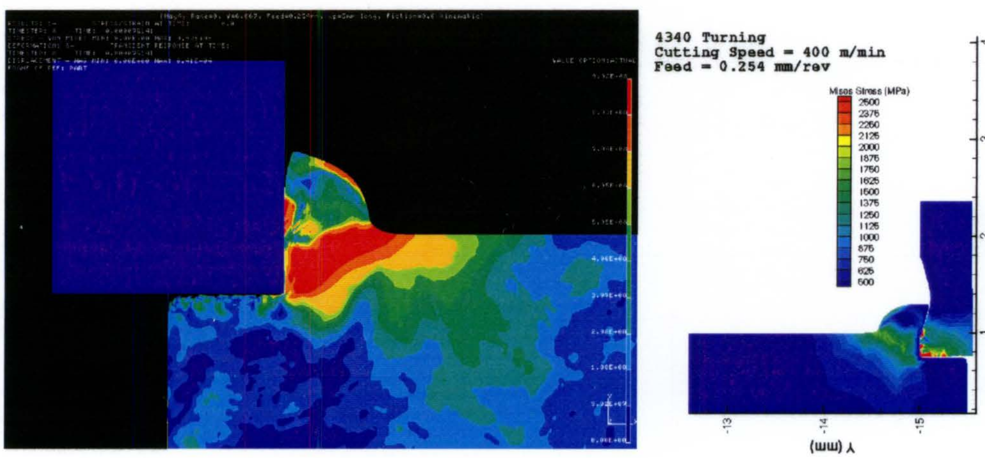

Figure 5.20 A comparison of plastic strain at early stages of chip formation as modeled by both H3dmap and 3rd Wave Systems under similar cutting conditions.

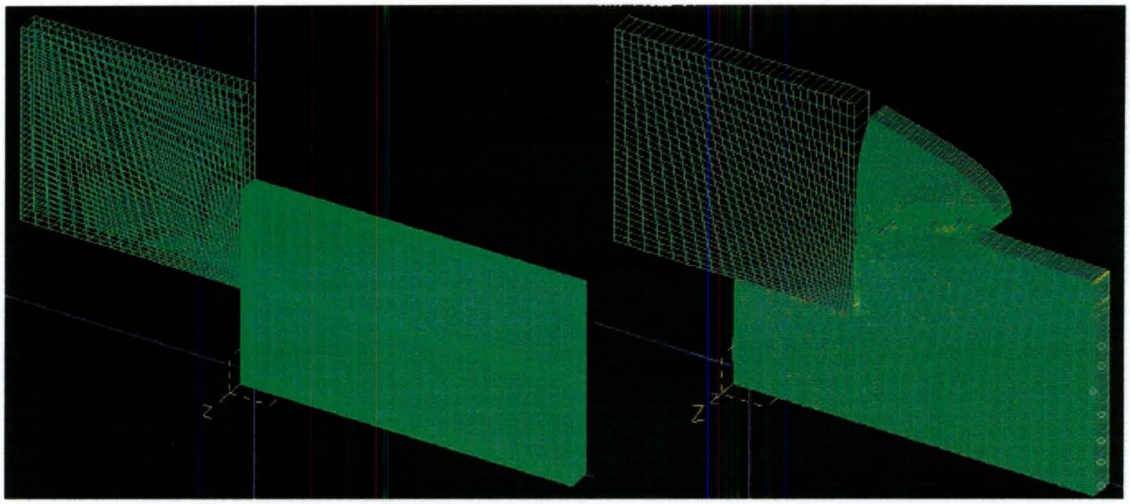

Figure 5.21 A 3-dimensional plot of both the un-deformed and the deformed workpiece and tool mesh at 0.0 and 6.0E-5 seconds respectively.

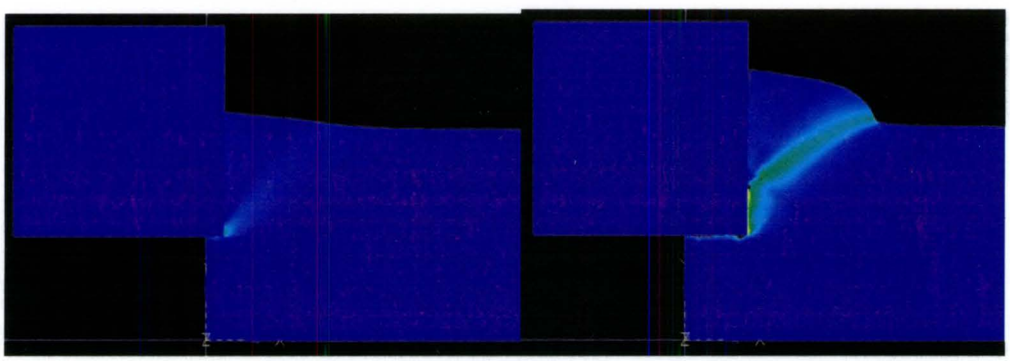

Figure 5.22 Plots of effective plastic strain at different stages of segmented chip formation demonstrating different stages of shear localization.

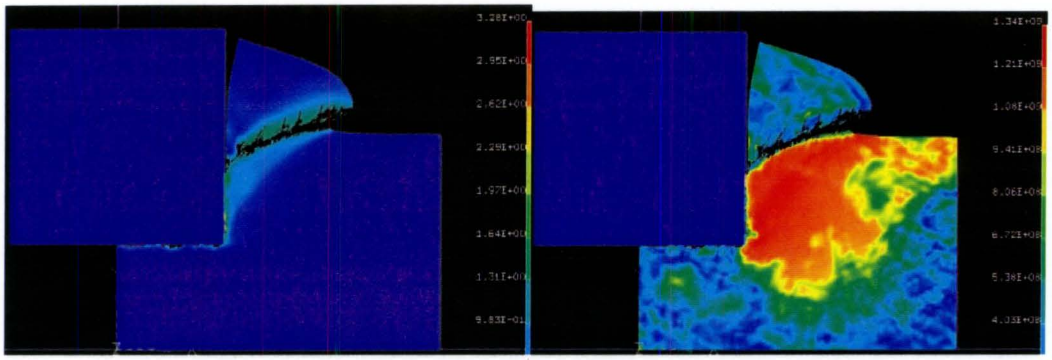

Figure 5.23 Plots of effective plastic strain and Von-Mises stress at 6.0E-5 seconds demonstrating segmented chip formation.

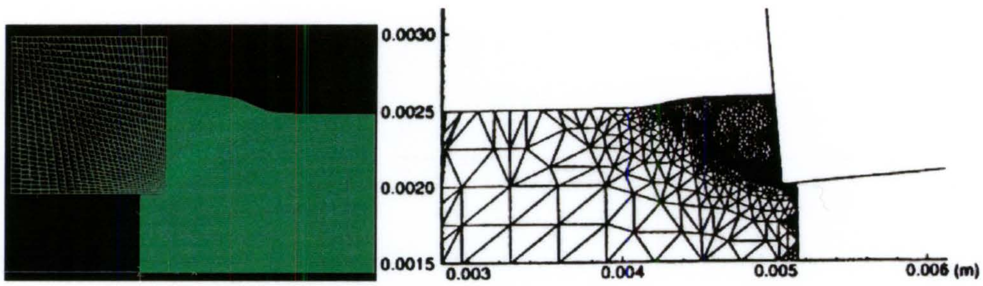

Figure 5.24 A comparison of deformed meshes at initial stages of segmented chip formation as generated by H3dmap and by Marusich and Ortiz (1995) respectively under similar cutting conditions.

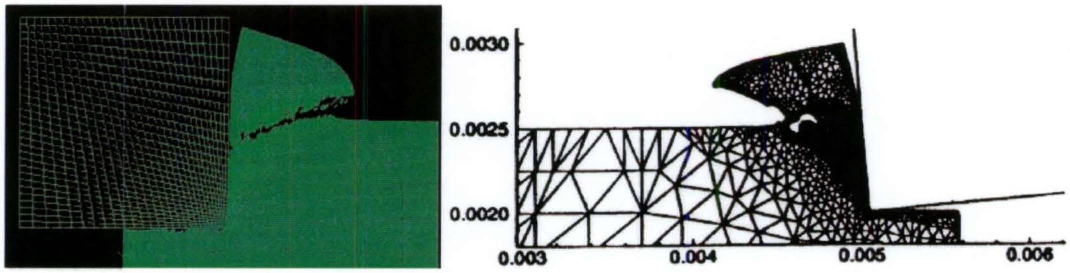

Figure 5.25 A comparison of deformed meshes at final stages of segmented chip formation as generated by H3dmap and by Marusich and Ortiz (1995) respectively under similar cutting conditions.

CHAPTER 6

CONCLUSIONS

The simulation of both continuous and segmented chip formation using explicit transient finite element methods is possible. Benchmarking comparisons with literature and commercial modeling software simulations are made and quantified in terms of strains, temperatures, residual stresses, and the various components of stress. The accurate prediction of the physical processes involved was achieved using software modified by the author and affiliated research group. Adiabatic shear localization was present in the simulation of cyclic chip formation. Material deformation and associated phenomenon were modeled using an appropriate Johnson Cook material model. Results were compared with a benchmarked commercial package obtaining good agreement in an orthogonal idealization.

Solution stability of the finite element solver applied to machining was quite low without the implementation of an adaptive remeshing scheme and a revised the contact algorithm. Thermal mechanical coupling, the simulation of coolant application, the application of friction based on experimental wear data, and volumetric remeshing are currently being implemented. Future recommendations include implementation of methods of crack propagation and generation without volumetric losses, an adaptive contact algorithm with associated node surface area tracking, machine tool and workpiece

REFERENCES

T. Shirakashi and K. Maekawa, "Recent Progress of Computer Aided Simulation of Chip Flow and Tool Damage in Metal Machining", Proc. Instn. Mech. Engrs., vol. 210, pp. 233-242, 1996.

T. Obikawa and H. Sasahara, "Application of Computational Machining Method to Discontinuous Chip Formation", Trans. ASME, J. Manuf. Sci. Eng., vol. 119, pp. 667-674, 1997.

B. Zhang and A. Bagchi, "Finite Element Simulation of Chip Formation and Comparison with Machining Experiment", Trans. ASME, J. Eng. Ind., vol. 116, pp. 289-297, 1994.

H. Ernst, "Physics of Metal Cutting", Machining of Metals, ASM, p. 24, 1938.

E. H. Lee, B. W. Shaffer, J. Applied Mechanics, vol. 18, p. 405, 1951.

M. E. Merchant, J. Applied Physics, vol. 16, no. 5, part I p. 267, part II p. 318, 1945.

M. C. Shaw, "Metal Cutting Principals", Chapt. 3, Clarendon Press, Oxford, 1984.

M. A. Elbestawi, A. K. Srivastava, and T. I. El-Wardany, "A Model for Chip Formation During Machining of Hardened Steel", Annals of CIRP, vol. 45. no. 1, pp. 71-76, 1996.

R. F. Recht, "Catastrophic Thermoplastic Shear", Trans. ASME, vol. 86, pp. 189-193, 1964.

R. Komanduri, Z. B. Hou, "Modeling of Thermomechanical Shear Instability in Machining", Int. J. Mech. Sci., vol. 39, no. 11, pp. 1273-1314, 1997.

M. C. Shaw and A. Vyas, "The Mechanism of Chip Formation with Hard Turning Steel", Annals of Cirp, 1998.

J. C. Jaeger, "Moving Sources of Heat and the Temperature at the Sliding Contacts", Proc. Roy. Soc. NSW, vol 76, pp. 203-224, 1942.

R. G. Sauvé and D. R. Metzger, "Advances in Dynamic Relaxation Techniques for Nonlinear Finite Element Analysis", Trans. ASME, J. Pres. Ves. Tech., vol. 117, pp. 170-176, 1995.

H. Sasahara, T. Obikawa, and T. Shirakashi, "FEM Analysis on Three Dimensional Cutting-Analysis on Large Deformation Problem of Tool Entry", Int. J. Japan Soc. Prec. Engng., 1994, vol. 28, no. 2, pp. 123-128, 1994.

T. Obikawa, E. Usui, "Computational Machining of Titanium Alloy-Finite Element Modeling and a Few Results", Trans. ASME, J. Manuf. Sci. Eng., vol. 118, pp. 208-215, 1996.

G. Meir, J. Hashemi, P. C. Chou, "Finite-Element Simulation of Segmented Chipping in High-Speed Machining", Con. Adv. Machin. Tech. II, Soc. Manuf. Engs. Feb 16-18, Phoenix, Arizona, 1988.

J. S. Strenkowski, J. T. Carroll, III, "A Finite Element Model of Orthogonal Metal Cutting", Trans. ASME, J. Eng. Ind., vol. 107, pp. 349-354, 1985.

T. D. Marusich and M. Ortiz, "Modeling and Simulation of High-Speed Machining", Int. J. Num. Meth. Eng., vol. 38, pp. 3675-3694, 1995.

R. Komanduri and T. Schroeder, "On the Catastrophic Shear Instability in High-Speed Machining of an AISI 4340 Steel", Trans. ASME, J. Eng. Ind., vol. 104, pp. 121-131, 1982.

W. Lee and G. Yeh, " The Plastic Deformation Behavior of AISI 4340 Alloy Steel Subjected to High Temperature and High Strain Rate Loading Conditions", J. Mat. Proc. Tech., vol. 71, pp. 224-234, 1997.

M. R. Lovell, S. Bhattacharya, and R. Zeng, "Modeling of Orthogonal Machining Processes for Variable Tool-Chip Interfacial Friction Using Explicit Dynamic Finite Element Methods", CIRP International Workshop on Modeling of Machining Operations, Atlanta, Georgia, USA, May 19, 1998.

Lee and Wang,"High Strain Rate Testing and Constitutive Modeling", 1997.

F. Zok and J.D. Embury, "The Influence of Hydrostatic Pressure on Fracture", Ph.D. Dissertation, McMaster University, Hamilton, Ontario, 1988.

R. G. Sauvé, "H3dmap Version 6.2 User Documentation and Manual" Applied Mechanics Development Component Integrity Department, Ontario Power Technologies, 1999.

3rd Wave Systems Inc., "Third Wave AdvantEdge Demo Version 3.2", 7301 Ohms Ln. - Suite 580, Minneapolis, USA, 1999.

R. Komanduri and R. H. Brown, "On the Mechanics of Chip Segmentation in Machining", Trans. ASME, J. Eng. Ind., vol. 103, pp. 33-51, 1981.